

Carbon measurements in two ultra-faint dwarf galaxies: Grus II and Tucana IV

Valentina Verdiani^{1,2}, Ása Skúladóttir^{1,2}, Romain Lucchesi^{1,2}, Alessio Mucciarelli^{3,4}, Davide Massari⁴, Giuseppina Battaglia^{5,6}, José María Arroyo-Polonio^{5,6}, Eline Tolstoy⁷, Sara Covella³, Salvatore Taibi⁸

¹ Università degli Studi di Firenze, Via G. Sansone 1, I-50019 Sesto Fiorentino, Italy.
e-mail: valentina.verdiani1@unifi.it

² INAF/Osservatorio Astrofisico di Arcetri, Largo E. Fermi 5, I-50125 Firenze, Italy

³ Dipartimento di Fisica e Astronomia, Alma Mater Studiorum, Università di Bologna, Via Gobetti 93/2, 40129 Bologna, Italy

⁴ INAF, Osservatorio di Astrofisica e Scienza dello Spazio, Via Gobetti 93/3, 40129 Bologna, Italy

⁵ Instituto de Astrofísica de Canarias, Calle Vía Láctea s/n, 38206 La Laguna, Santa Cruz de Tenerife, Spain

⁶ Universidad de La Laguna, Avda. Astrofísico Francisco Sánchez, 38205 La Laguna, Santa Cruz de Tenerife, Spain

⁷ Kapteyn Astronomical Institute, University of Groningen, PO Box 800, 9700 AV Groningen, The Netherlands

⁸ Institute of Physics, Laboratory of Astrophysics, École Polytechnique Fédérale de Lausanne (EPFL), 1290 Sauverny, Switzerland

ABSTRACT

The ultra-faint dwarf galaxies (UFDs) are some of the oldest and most metal-poor environments in the Local Group. In particular, they are predicted to host the first stars (only H and He) that lit up in our Universe. No metal-free stars have been found to date, but their chemical products can be observed on the surfaces of the ancient second-generation stars such as the carbon-enhanced metal-poor stars (CEMP-no, $[C/Fe] > +0.7$). However, in each UFD there are only a few stars bright enough for spectroscopic follow-up, therefore it is crucial to study as many of these systems as possible. Here we follow up stars belonging to two recently discovered UFDs, Grus II and Tucana IV. The spectra analyzed were obtained with the multi-object spectrograph FLAMES/Giraffe at the Very Large Telescope (VLT). This includes spectra in two wavelength ranges: red spectra around the Ca II triplet (8498 Å, 8542 Å, 8662 Å) used to derive radial velocity and $[Fe/H]$, and blue spectra covering the CH band at ~ 4300 Å. In total, we analyzed 21 spectra of member candidates for Grus II and 17 for Tucana IV, including both Red Giant Branch (RGB) and Horizontal Branch (HB) stars. We identified 13 members in Grus II (thereof 8 RGB stars) and 7 members in Tucana IV (thereof 3 RGB stars). Among the RGB stars in Grus II, we found three CEMP-no stars at $[Fe/H] \approx -3$ and $[C/Fe] > +1$ and two CEMP-no stars at slightly higher $[Fe/H]$ and $[C/Fe] > +0.7$. In Tucana IV, we found one CEMP-no star ($[Fe/H] = -2.75$ and $[C/Fe] = +0.83$). This project, along with future investigations of CEMP stars in UFDs, allows us to study the impact of the first stars in these ancient and primitive systems and consequently the first chemical enrichment that occurred in the Universe.

Key words. Galaxies: ultra-faint dwarf galaxies - Galaxies: abundances - Stars: metal-poor stars

1. Introduction

The discovery of the ultra-faint dwarf galaxy (UFDs, $L < 10^5 L_\odot$, Simon 2019) satellites of the Milky Way has piqued a wide interest: these systems are very metal-poor and among the most ancient objects in the Local Group (e.g. Salvadori & Ferrara 2009; Simon 2019). Several studies affirm that the UFDs could be the first mini-halos that hosted the first stars (Pop III, Bovill & Ricotti 2009; Salvadori et al. 2015). These predictions are corroborated by the star formation histories of these systems (Brown et al. 2014; Gallart et al. 2021) that suggest that the star formation only lasted for the first \sim Gyr of the Universe.

Pop III stars are formed from a gas cloud with a primordial chemical composition (H, He). Due to the lack of metals, the roto-vibrational transitions of the H₂ molecules are the only cooling channel available ($T \sim 10^4$ K, Tegmark et al. 1997). Since this cooling channel is not efficient, the first stars are predicted to be more massive than present-day stars (e.g. Hirano et al. 2014). In a few Myr, these massive Pop III stars released into the interstellar medium (ISM) the chemical elements heavier than He through supernova (SN) explosions. Thus, Pop III stars are responsible for the early chemical enrichment of the

primordial ISM and play a key role in the onset of the reionization of the Universe (e.g. Bromm & Yoshida 2011). To date, the first stars have not been directly observed and we don't know if low-mass long-lived Pop III stars were able to form since in this case they should be observable in the Local Group (e.g. Rossi et al. 2021).

Even though Pop III stars have never been found at the present moment, the galactic archaeology studies of UFDs are fundamental to understanding the first chemical enrichment of the Universe since there is a high probability that they can host the descendants of Pop III stars (Frebel & Bromm 2012). Due to UFDs low gravitational potential well, the chemical products of the most energetic SNe are unlikely to be retained in the galaxy environment, resulting in a low fraction of metals and consequently a quenched star formation (Rossi et al. 2024). However, UFDs are able to retain the chemical products of the lowest-energy SNe. The recent discovery of an extremely metal-poor second-generation star in the Pictor II UFD (Chiti et al. 2025) supports this hypothesis.

When investigating Pop III descendants, the carbon-enhanced metal-poor stars (CEMP-no; $[C/Fe] > 0.7$, with no Ba enhancement) are of special interest: they are the descendants of

Pop III stars exploding as faint supernovae ($E \lesssim 10^{51}$ erg) which pollute the environment mainly with lighter elements, such as C, resulting in very high [C/Fe] ratios (Iwamoto et al. 2005). This peculiar chemical pattern will be preserved in the photosphere of the descendant stars which can survive until the present day and are observed both in the Milky Way and its satellites (e.g. Aoki et al. 2007; Norris et al. 2010; Skúladóttir et al. 2015). We note that other formation scenarios have been proposed to explain the CEMP-no stars, such as inhomogeneous internal mixing after the first SNe (Hartwig & Yoshida 2019), the accretion of C-rich gas from a companion in binary systems (Komiya et al. 2020), or metal-pollution due to second-generation star explosions (Jeon et al. 2021).

Another class of CEMP stars is mostly found in binary systems (Starkenburg et al. 2014; Hansen et al. 2015) and they have been enriched both in C and s-process elements (like Ba) by an Asymptotic Giant Branch (AGB) companion. These are called CEMP-s stars (see e.g. Beers & Christlieb 2005) and are not representative of the environment in which they were born, i.e. they do not descend from the Pop III stars. CEMP-s stars are defined as those with $[\text{Ba/Fe}] > 1$ and are typically found at higher [Fe/H] compared to CEMP-no stars (Norris et al. 2013). Additionally, they can be recognized because they present higher absolute carbon abundances, A(C), than CEMP-no stars (Bonifacio et al. 2015). Additionally, we mention the CEMP-r stars class, i.e. the CEMP stars enriched with r-process elements (such as Eu) and CEMP-r/s stars, which are enhanced both in r- and s-process elements. Both of these objects are significantly rarer than CEMP-s and CEMP-no stars. (Beers & Christlieb 2005).

The fraction of CEMP-no stars increases towards lower metallicities (e.g. Beers & Christlieb 2005; Lee et al. 2013; Placco et al. 2014), and indeed in the metal-poor UFDs the fraction of these Pop III descendants is high (Norris et al. 2010; Salvadori et al. 2015; Ji et al. 2020a). The CEMP fraction trend in the Milky Way halo is similar to that of the UFDs. Although several CEMP-no stars have been found in dwarf spheroidal galaxies (dSphs) (e.g. Skúladóttir et al. 2015; Susmitha et al. 2017, Cuadra et al. in prep), their fraction seems to be low (e.g. Starkenburg et al. 2013). From low-resolution spectra ($R \approx 2000$), Chiti et al. (2018) reported that the CEMP-no fraction in Sculptor is rising towards lower [Fe/H], reaching values similar to the Milky Way. However, this result is not seen in any of the higher resolution studies in the Sculptor dSph (Frebel et al. 2010; Tafelmeyer et al. 2010; Starkenburg et al. 2013; Simon et al. 2015; Jablonka et al. 2015; Skúladóttir et al. 2015; Skúladóttir et al. 2021; Skúladóttir et al. 2024). Furthermore, a recent compilation of literature data by Lucchesi et al. (2024) shows a significantly lower fraction of CEMP-no stars in dSphs. However, the uncertainties are large, suggesting that further investigation is needed, especially at the lowest metallicities.

In UFDs, spectroscopic follow-up is feasible only for the few brightest stars, so statistics are lacking. Therefore, in this work we targeted Red Giant Branch (RGB) and Horizontal Branch (HB) stars in two recently discovered UFDs, Grus II and Tucana IV (Drlica-Wagner et al. 2015), visible from the Southern Hemisphere. The stellar masses of the galaxies are $M_* = 3.4^{+0.3}_{-0.4} \times 10^3 M_\odot$ for Grus II and $M_* = 2.2^{+0.4}_{-0.3} \times 10^3 M_\odot$ for Tucana IV, and their heliocentric distances are respectively $d = 53 \pm 5$ kpc and $d = 48 \pm 4$ kpc (Drlica-Wagner et al. 2015). Until today, these two UFDs are still poorly studied. Massari & Helmi (2018) and Pace & Li (2019) were the first to determine their kinematic properties and to study their orbit around the Milky Way. Simon et al. (2020) analyzed some stars in these galaxies, deriving the radial velocities (that is their heliocentric line-of-

sight velocities), the metallicities and properties of the galaxies, such as their velocity dispersion and orbits around the MW. Additionally, Hansen et al. (2020) determined detailed chemical abundances of the brightest stars in Grus II. However, a derivation of carbon abundances to determine the number of CEMP stars in these two UFDs has never been done. In this work, we derived the line-of-sight velocity, metallicity and carbon abundance measurements of candidate targets of stars belonging to Grus II and Tucana IV, aiming to identify member stars and investigate [C/Fe] at low [Fe/H] in these galaxies to identify CEMP stars.

2. Observational data

We selected the spectroscopic targets based on the mean proper motion of the two galaxies as found by Pace & Li (2019). Candidate members were chosen among bright stars having a proper motion consistent with the mean galaxy motion within 3σ . The target stars were observed with the multi-object spectrograph FLAMES/Giraffe at the Very Large Telescope (VLT; ESO program IDs 0103.B-0163, 105.205T, PI D. Massari). The HR21 setting was used to cover the Ca II triplet region (8498 Å, 8542 Å, 8662 Å) in the red, while the CH molecular band (~ 4300 Å) in the blue was covered by the LR2 grating (see Table 1). The exposure time of each observing block is 3600 s. Every star in Tucana IV got 4h of observations for both the red and blue, while Grus II potential members got either 2h or 4h (see Table E.1). The first observation was carried out in July 2019, the second from July to September 2021. Figure 1 shows examples of red and blue spectra in Grus II. The sample contains both stars belonging to the RGB and HB (Figure 1). For each exposure obtained with HR21, we cross-correlated the position of the observed sky emission lines against a sky spectrum selected among the sky spectra of our dataset. This check was performed for each individual exposure before co-adding together the spectra of the same target. We found typical differences (in absolute value) smaller than 0.4 km s^{-1} , corresponding to one-fourth of the GIRAFFE pixel. Moreover, no significant systematic offset was found, as the average difference was $+0.05 \text{ km s}^{-1}$ with a σ of 0.14 km s^{-1} . We also checked possible fiber-dependent effects like those mentioned in Jenkins et al. (2021), but we did not find any significant patterns.

The proper motions (pmra and pmdec, in this work $\mu_\alpha \cos(\delta)$ and μ_δ), the right ascension (RA), the declination (DEC) in J2000, the magnitudes (phot_g_mean_mag, phot_bp_mean_mag, phot_rp_mean_mag, in this work G, BP, RP) and other parameters were taken from the Gaia Data Release 3 (Gaia DR3) and are listed in Table E.2 and Table E.3. Figure 2 shows the color-magnitude diagram (CMD) of the spectroscopic sample, along with likely members based on Gaia eDR3 from the selection of Battaglia et al. (2022). Moreover, in Appendix A, we show the CMD with the isochrones overplotted (Figure A.1).

The spectra were reduced using the ESO pipeline developed for FLAMES-GIRAFFE spectra¹. The pipeline workflow performs for each individual observation bias-subtraction, flat-fielding, wavelength calibration using a standard Th-Ar lamp, and spectral extraction. The accuracy of the wavelength calibration for the spectra observed with HR21 was checked by measuring the position of several sky lines (not available in the LR2 spectra). For each exposure, the stellar spectra were corrected for the sky background contribution by subtracting a spectrum

¹ https://www.eso.org/sci/software/pipe_aem_main.html

Table 1: Observational settings.

FLAMES setting	Resolution	λ [Å]
LR2	6 000	3960 - 4570
HR21	18 000	8480 - 8980

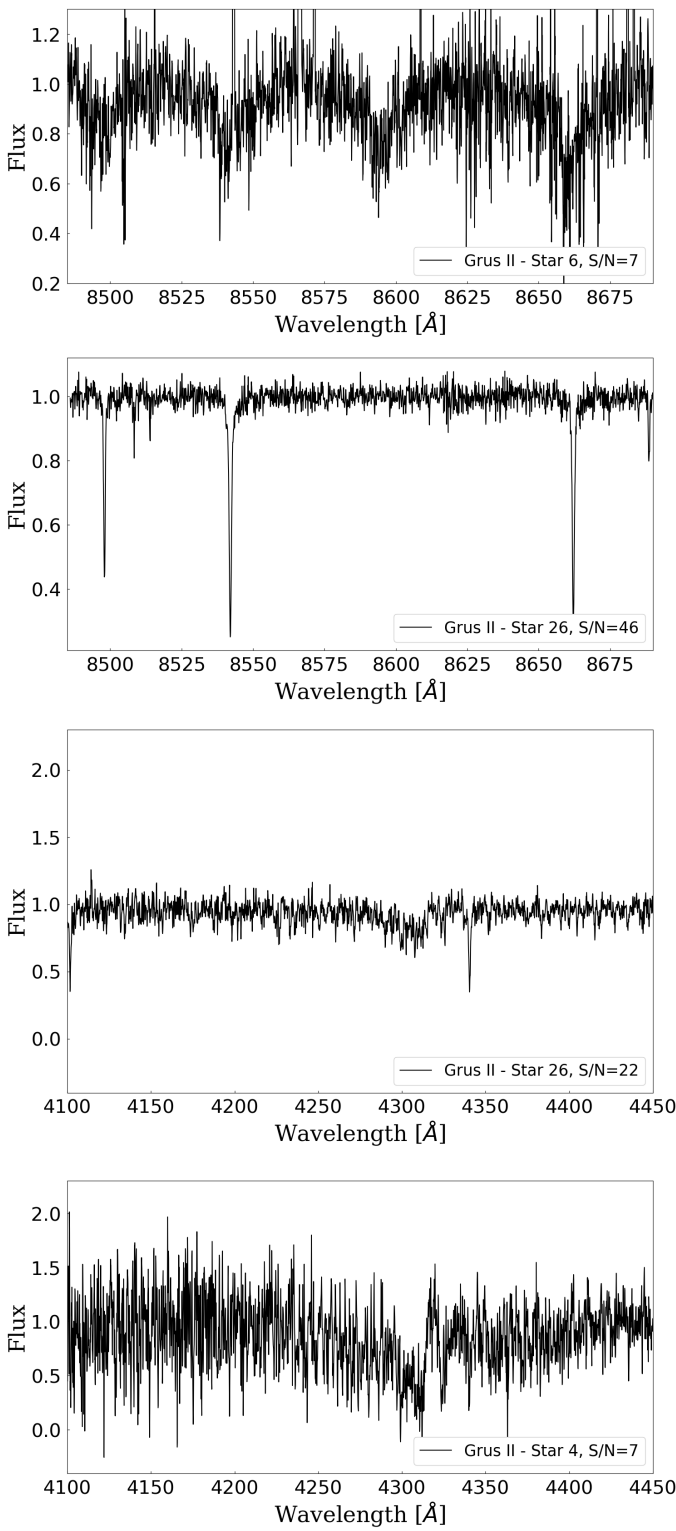


Fig. 1: Example of spectra of our target stars. **Top:** star 6 in Grus II, a hot HB star whose spectrum is dominated by Paschen lines. **Middle:** the Ca II triplet (2nd panel) and the CH band (3rd panel) spectra of the RGB star 26 in Grus II, **Bottom:** CH band spectrum of the RGB star 4 in Grus II.

obtained by median-averaging together all the individual sky spectra. After performing the heliocentric corrections, the spec-

tra were normalized and co-added with the removal of cosmic rays.

After this procedure, we determined the signal-to-noise ratio (S/N) by deriving the variance of the flux in line-free regions. In the case of the blue spectra, the S/N was difficult to measure due to lack of line-free regions (see Figure 1, bottom panel), and the listed S/N in the blue should therefore be considered as a lower limit (Table E.1).

3. Atmospheric parameters and stellar models

3.1. Effective temperature

To derive the effective temperatures the following formula was used (Mucciarelli & Bellazzini 2020):

$$T_{\text{eff}} = \frac{5040}{\theta} \quad (1)$$

with θ defined as:

$$\theta = b_0 + b_1 C + b_2 C^2 + b_3 [\text{Fe}/\text{H}] + b_4 [\text{Fe}/\text{H}]^2 + b_5 [\text{Fe}/\text{H}] C \quad (2)$$

where $b_0 \dots b_5$ are the parameters for giant stars from Mucciarelli et al. (2021) and C represents the colors $(\text{BP} - \text{RP})_0$, $(\text{BP} - \text{G})_0$, $(\text{G} - \text{RP})_0$, obtained from the magnitudes in the G, BP and RP bands provided by Gaia. This calibration is not adequate for hot stars ($T_{\text{eff}} > 6500$ K) since Equation 2 holds for RGB stars, but it was used in this work with the only aim of identifying the HB stars. The spectra were then confirmed as belonging to hot stars by checking for the presence of strong Paschen lines (see Figure 1, top panel). Moreover, we compared the position of the stars in the color-magnitude diagram (Figure 2 and Figure A.1) with our results to confirm a reliable identification of HB stars, all having $(\text{BP} - \text{RP}) \lesssim 0.5$. The colors are extinction and reddening corrected: the extinction factor is

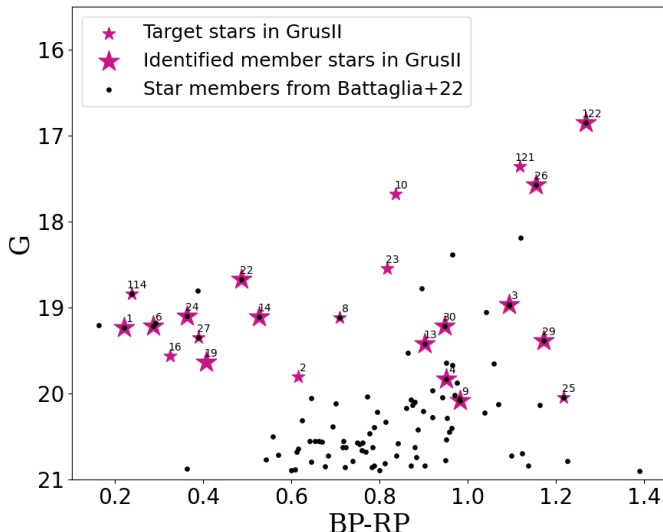
$$A_X = A_0 k_X \quad (3)$$

where X are the magnitudes (G, BP, RP) and k_X is defined by Equation 1 in Gaia Collaboration et al. (2018). The color-independent extinction coefficient is provided by Gaia: $A_0 = 3.1 E(B - V)$, where $E(B - V)$ is the color excess. The term $(\text{BP} - \text{RP})_0$ that appears in the definition of k_X was derived by performing four iterations, with $(\text{BP} - \text{RP})_0$ equal to $(\text{BP} - \text{RP})$ measured directly by Gaia as the initial guess. The results were used to derive the A_X coefficients and therefore the real magnitudes and colors.

The final adopted T_{eff} is the average of the three T_{eff} obtained from the three colors. In the Appendix, Table E.2 and Table E.3 report the corrected colors and the mean effective temperature of every star of the sample. The error on the T_{eff} :

$$\sigma_{T_{\text{eff}}} = \sqrt{\sigma_1^2 + \sigma_2^2} \quad (4)$$

Grus II



Tucana IV

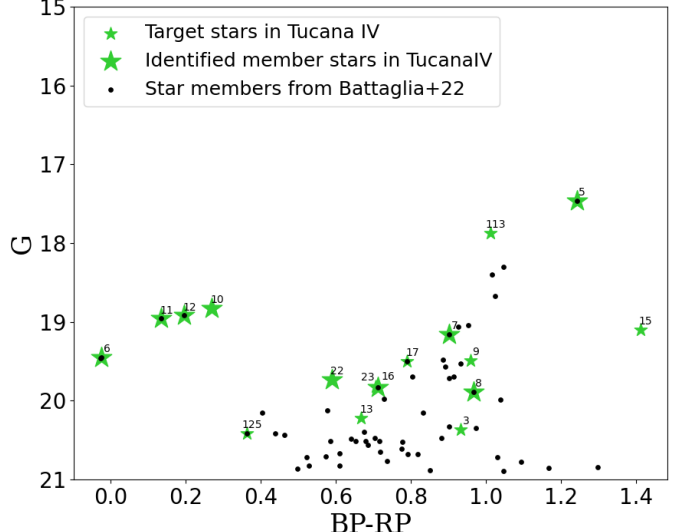


Fig. 2: Color-magnitude diagram of Grus II (left panel) and Tucana IV (right panel). The star symbols indicate our FLAMES/GIRAFFE targets, larger symbols are the member stars determined in Section 4.1, and black small circles represent possible members from the catalog by Battaglia et al. (2022) based on Gaia eDR3 measurements. Numbers are the star IDs (Table E.2 and Table E.3). Figure A.1 also shows the CMD with isochrones of different metallicities overplotted.

where $\sigma_1 = \frac{\sigma_{\text{std}}}{\sqrt{2}}$ is the error on the mean of the three color temperatures, while $\sigma_2 = \frac{s_1 + s_2 + s_3}{3}$ is the mean of the three errors associated to the colors ($s_1 = 83$ K, $s_2 = 83$ K and $s_3 = 71$ K.), which represents the intrinsic systematic error of the estimated method from Mucciarelli et al. (2021).

3.2. Surface gravity

The surface gravity is evaluated using the known Stefan-Boltzmann relation (see e.g. Skúladóttir et al. 2024):

$$\log g_* = \log g_\odot + \log \frac{M_*}{M_\odot} + 4 \log \frac{T_{\text{eff}}}{T_{\text{eff},\odot}} + 0.4 (M_{\text{bol},*} - M_{\text{bol},\odot}) \quad (5)$$

where $M_{\text{bol},*} = G_0 - (m - M) + BC$ is the bolometric magnitude and BC is the bolometric correction (derived using Eq. 7 in Andrae et al. 2018). The stellar mass considered is the typical one of the RGB stars in UFDs, i.e. $0.8 \pm 0.2 M_\odot$. The solar values used are $\log g_\odot = 4.44$, $T_{\text{eff},\odot} = 5772$ K and $M_{\text{bol},\odot} = 4.74$.

The error on the $\log g_*$ is found assuming negligible errors on the solar parameters:

$$\sigma_{\log g_*} = \sqrt{\sigma^2 \left(\log \frac{M_*}{M_\odot} \right) + 4 \sigma^2 \left(\log \frac{T_{\text{eff},*}}{T_{\text{eff},\odot}} \right) + 0.4 \sigma^2 (M_{\text{bol},*})} \quad (6)$$

3.3. Microturbulence velocity

From Anthony-Twarog et al. (2013), we used the empirical relation:

$$v_{\text{turb}} = 2.0 - 0.2 \log g_* \quad (7)$$

The error on the v_{turb} is found with

$$\sigma_{v_{\text{turb}}} = \sqrt{(0.2 \sigma_{\log g_*})^2 + \sigma_{v_{\text{turb},\text{rms}}}^2} \quad (8)$$

where $\sigma_{v_{\text{turb},\text{rms}}} = 0.17$ km s⁻¹, which represents the average scatter between the empirical relation and the measurements (Carretta et al. 2004).

3.4. Stellar models and synthetic spectra

Synthetic spectra are generated by using a grid of Model Atmospheres with a Radiative and Convective Scheme (MARCS) (Gustafsson et al. 2008) combined with Turbospectrum (Plez 2012). The grid of MARCS 1D atmosphere models is downloaded with the *Standard composition*, that is, including the classical α -enhancement of +0.4 dex at low metallicity, from the MARCS web site² (Gustafsson et al. 2008), and interpolated using Thomas Masseron's *interpol_models* code for the given parameters of each star. Synthetic spectra are computed for each model, starting from solar chemical abundance ratios ([X/Fe]=0) and an estimated metallicity of -2.0. This first estimate of [Fe/H] is used to generate the synthetic spectrum for the derivation of the radial velocity, which is not sensitive to the exact assumed [Fe/H].

Employing the χ^2 minimization method, we find the best fit to an observed spectrum to derive the radial velocities (Section 4.1) and chemical abundances (Section 5).

4. Membership determination

4.1. Radial velocities

After an accurate continuum level identification that allows us to normalize the stellar spectra, our aim was to determine the members among the target stars. We derived the radial velocity (v_{rad}) from the Ca II triplet lines using the minimization of the χ^2 method, i.e. iterating by shifting the observed spectrum with different values of v_{rad} in a range between ± 100 km s⁻¹ around the average of the galaxies (McConnachie 2012) in steps

² <http://marcs.astro.uu.se>

of 0.1 km s^{-1} until the best fit to a synthetic spectrum (created adopting the stellar parameters calculated in Section 3) is obtained (Figure 3). Figure 4 shows radial velocity distributions of Grus II and Tucana IV derived from the red spectra.

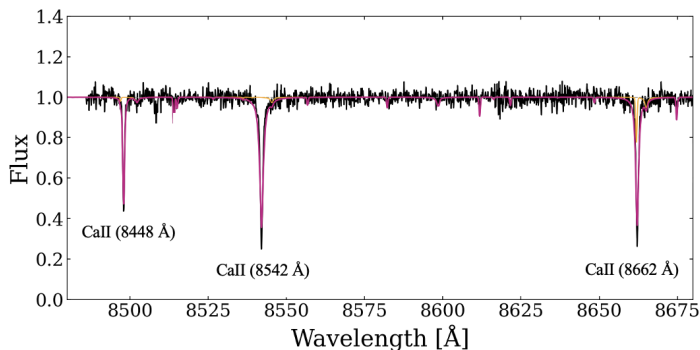


Fig. 3: The Ca II triplet of the star 26 in Grus II. The black line is the observed spectrum, the magenta line is the synthetic spectrum best fit to the radial velocity of the star.

The radial velocities of every targeted star we analyzed in Grus II and Tucana IV are listed in Table E.1 with corresponding uncertainties. Two stars (2 and 19) in Grus II were discarded from our analysis since their S/N was very low, preventing us from obtaining reliable measurements. Stars 1, 14 and 114 in Grus II and star 125 in Tucana IV do not have any available exposures in the red, therefore their radial velocities are only derived from the blue LR2 setting.

The errors on the radial velocity are found by performing Montecarlo simulations. Using a template spectrum, we made 1000 iterations by adding random Gaussian noise to obtain mock observed spectra at five fixed S/N (5, 15, 30, 50, 70 pix^{-1}). After defining an array of radial velocity in steps of 0.1 km s^{-1} , the best value of v_{rad} is found for all the Montecarlo spectra, comparing them with the best synthetic spectra of the stars in the sample. The distribution of the best values should be centered around 0, but the dispersion increases with lower S/N. Additionally, we tested this method using spectra with different stellar parameters and we obtained consistent results. The sigma of the distributions derived for these 5 fixed S/N values serves as a reference for performing a polynomial fit to the curve of the radial velocity error as a function of the S/N (typically $\sigma_{v_{\text{rad}}} \lesssim 0.4 \text{ km s}^{-1}$ for $S/N > 20 \text{ pix}^{-1}$, $\sigma_{v_{\text{rad}}} \sim 1.5 \text{ km s}^{-1}$ at $S/N \sim 10 \text{ pix}^{-1}$ and $\sigma_{v_{\text{rad}}} \sim 2.5 \text{ km s}^{-1}$ at $S/N \sim 5 \text{ pix}^{-1}$). Moreover, star 22 in Grus II is a special case since the Ca triplet lines are completely contaminated by the skylines: we derived the radial velocities of the two exposures using the Paschen line at $\sim 8600 \text{ Å}$. Since this is a broad line, we expected large uncertainty and indeed obtained an error of 5 km s^{-1} by visual inspection of the comparison between the observed and template spectra. Two separate polynomial fits were done for the RGB and HB member stars, since the spectra have different features (Figure 1).

Additionally, we derived the v_{rad} from the CH-band region for all the stars with LR2 spectra, obtaining the same member identification given by the red spectra. However, these measurements are less reliable since the spectra are of lower resolution (see Table 1), the S/N is typically lower than the red spectra and the CH-band contains many broad molecular features. Moreover, the radial velocity from broad lines, H_{δ} and the H_{γ} are less trustworthy than the ones obtained with the Ca II triplet. Furthermore, while the wavelength calibration in HR21 was checked by the positions of the location of the sky lines, there are no sky lines

available in the blue LR2 region. This is why the preferred procedure involves the narrower atomic lines of the Ca II triplet. The same procedure was used for the errors in the blue as for the red. However, since there are no skylines, the zero-point could not be verified, and therefore the systematic errors are not included in the estimated uncertainties. Figure C.1 compares the results of the radial velocity derived from the red and blue spectra.

4.2. Combining radial velocities with Gaia

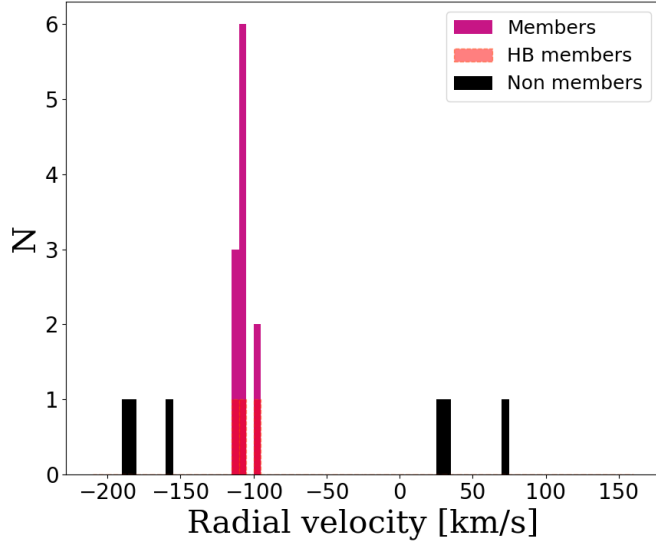
For the final member identification, we combined our measured radial velocities with information from Gaia. Figure 5 shows the proper motion in RA and DEC of the stars color-coded by the probability of membership and the average systemic proper motion of the galaxy from Battaglia et al. (2022). In Figure 6 are reported the histograms of the membership probability of our stars according to (Battaglia et al. 2022). The colored bars are the identified member stars, while the gray bars are the non-members. Figure 7 shows the positions of the stars color-coded by the radial velocity derived in Section 4.1. All these results are discussed in detail in the following subsections.

4.2.1. Grus II

Since the radial velocity distribution of Grus II shows a large velocity offset with respect to Milky Way stars (see Figure 4), the eleven members we identified in Grus II are clearly separated from the non-members. The systemic radial velocity of the galaxy is obtained by calculating the weighted mean of the radial velocity of the individual member stars, $v_{\text{sys}} = -106.3 \pm 0.1 \text{ km s}^{-1}$, while the velocity dispersion is $\sigma = 4.7 \pm 1.0 \text{ km s}^{-1}$. After the derivation of radial velocity and establishing the star members belonging to the galaxies, we compared our results with the membership probability based on Gaia eDR3 only, reported in Battaglia et al. (2022), see Figure 6. According to this catalog, all of Grus II star members we found have a probability higher than 80% of belonging to the galaxy. The non-member stars, on the other hand, exhibit a probability lower than 60%, (Figure 6). We note that the HB star 22 shows some signature of variability in radial velocity (see Section C).

We note that stars 1, 14 and 114 (all HB stars) have only blue spectra available (see Section 4.1). Therefore we derive the radial velocities from the CH-band: the values are $v_{\text{rad}} = -98.8 \pm 0.5 \text{ km s}^{-1}$, $v_{\text{rad}} = -104.0 \pm 1.2 \text{ km s}^{-1}$ and $v_{\text{rad}} = -22.4 \pm 1.9 \text{ km s}^{-1}$ respectively. The proper motions of stars 1 and 14 ($\mu_{\alpha} \cos(\delta) = 0.273 \pm 0.221$ and $\mu_{\delta} = -1.624 \pm 0.213$ and $\mu_{\alpha} \cos(\delta) = 0.496 \pm 0.195$ and $\mu_{\delta} = -1.527 \pm 0.198$, respectively) and their position on the CMD (Figure 2) support the identification as members, while star 114 is classified as a non-member since its radial velocity differs $>5\sigma$ from the peak of the distribution. Therefore, we have confirmed in total 13 stars as members in Grus II. However, to ensure self-consistency of our results, we do not include these stars (with only blue spectra) in Figure 4 and Figure 5 or in the following analysis. The proper motions of the member stars of Grus II are shown in Figure 5 and they are all consistent with the systemic proper motions. Moreover, we do not see any velocity gradient that indicates a tidal disruption of the galaxy (see Figure 7).

Grus II



Tucana IV

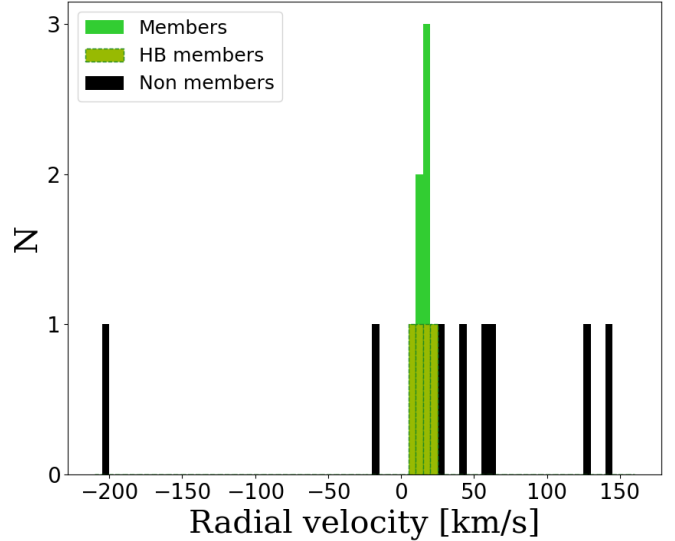
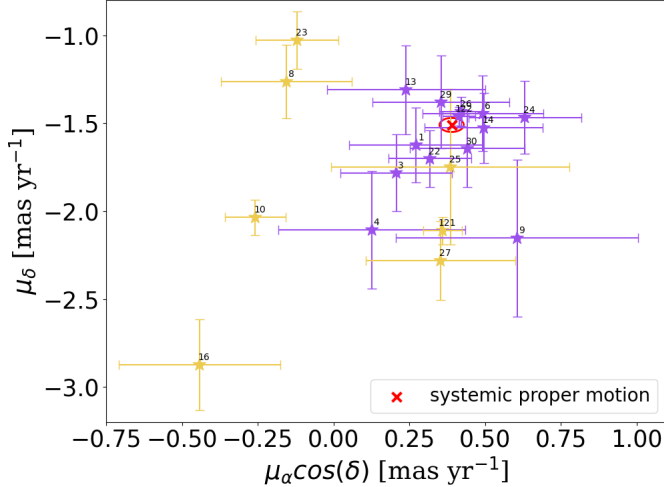


Fig. 4: Radial velocity distribution of Grus II (left panel) and Tucana IV (right panel). The black bars represent the non-members, the colored ones are the members. The shaded bars are the HB members, which do not present any significant difference or offset from the RGB stars in radial velocity. We only include stars with red spectra available, but we note that the HB stars 1 and 14 in Grus II are members based only on measurements from blue spectra (Table E.1).

Grus II



Tucana IV

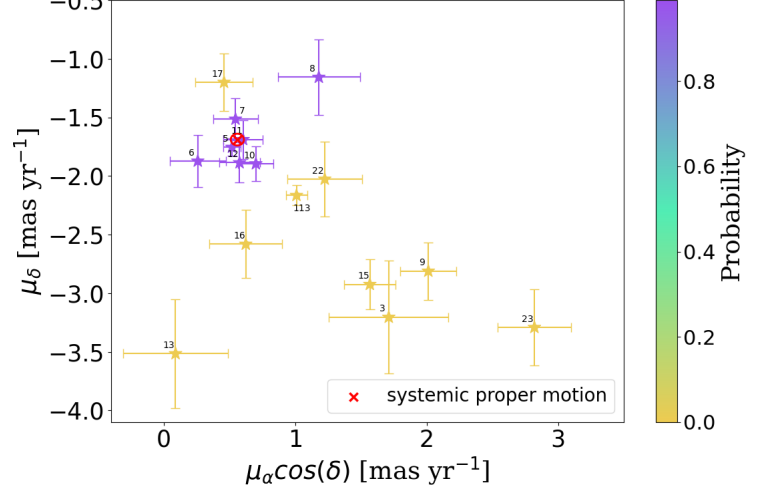


Fig. 5: Proper motions of the stars in Grus II and Tucana IV from Gaia DR3. The stars are color-coded according to the membership probability based on Battaglia et al. (2022). The red cross is the systemic proper motion (Battaglia et al. 2022), the red ellipse corresponds to 1σ , which is the error on the mean proper motions.

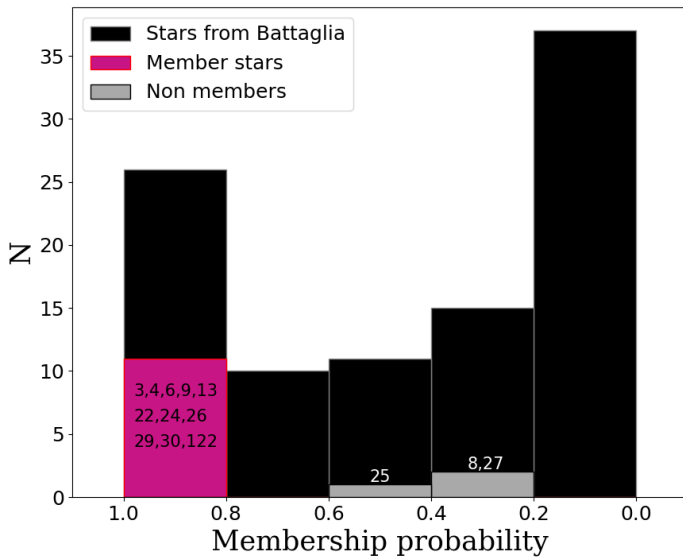
4.2.2. Tucana IV

The mean radial velocity of Tucana IV is relatively close to zero (see Figure 4), leading to similar radial velocity between members and non-members due to Galactic contamination. Moreover, we do not know the impact of binary stars, therefore we did not exclude a priori the stars that differ less than 3σ from the center of the distribution (stars 9, 16, 17, 22 and 113), where here σ is the standard deviation of the distribution considering the certain and potential members identified in this part of the analysis. We found 12 stars within 50 km s^{-1} from the average radial velocity of Tucana IV. Here, we are performing a very broad membership assignment based only on the radial velocity information with the aim of not excluding potential mem-

bers in binary systems. This will now be refined to include also the probabilities of membership determined from Gaia, since we are aware that not all of the considered stars are binaries. Star 125 has only the blue LR2 exposures available, from which we obtain $v_{\text{rad}} = -40.0 \pm 2.5 \text{ km s}^{-1}$, which makes it likely a non-member (corroborated by its position on the CMD, see Figure 2). As previously mentioned, we will not include this star in further discussion to ensure self-consistency.

In the case of Tucana IV, we re-derived the membership probability adding the information of the radial velocity and the corresponding errors obtained in this work, following the approach explained in detail in Battaglia et al. (2022). This is shown in Figure 5. The stars that fall in the main peak of the

Grus II



Tucana IV

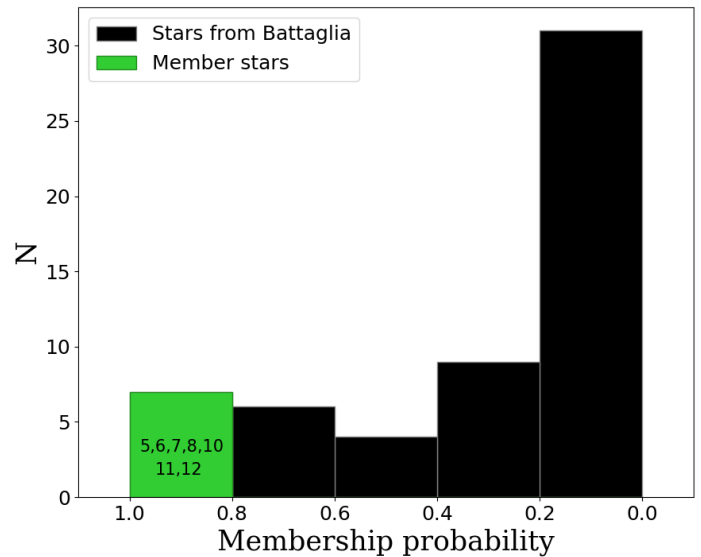
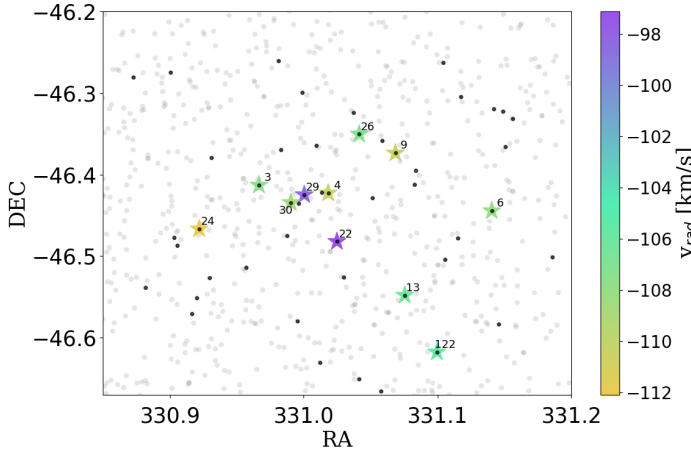


Fig. 6: Histograms of membership probability in Grus II and Tucana IV from Battaglia et al. (2022), showing our targets in colors (members) and gray (our non-members). We note that non-member stars 10, 16, 23, 121 in Grus II and 3, 13, 15, 23 in Tucana IV are not included in the Battaglia et al. (2022) catalog.

Grus II



Tucana IV

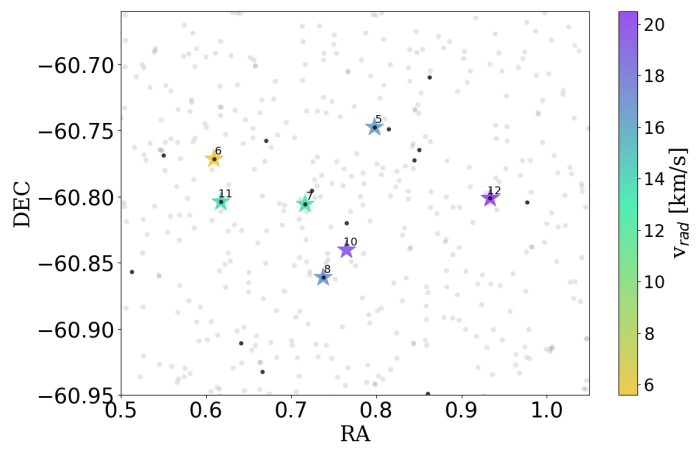


Fig. 7: Positions of our member stars color-coded by radial velocity.

radial velocity distribution have a probability $\sim 99\%$ to be members. We paid particular attention to 5 stars that have a radial velocity that differs more than 2σ from the average: stars 9, 16, 17, 22 and 113. According to Battaglia et al. (2022) method, these stars have a very low probability of being members. Furthermore, considering in particular their offset in radial velocity, we can conclude that these 5 stars are "unlikely members", as we do not expect all of them to be binaries. However, since the Gaia CMD and astrometry are moderately reasonable (see Figure 2 and Figure 5), we still analyzed them in Appendix B. The systemic radial velocity of Tucana IV is $v_{\text{sys}} = 16.2 \pm 0.2 \text{ km s}^{-1}$ and the velocity dispersion is $\sigma = 5.1 \pm 1.3 \text{ km s}^{-1}$.

Finally, by checking the position of the member and potential member stars color-coded by the radial velocity (Figure 7), we do not see any signatures of tidal disruption in this UFD.

5. Chemical abundance analysis

We performed this analysis for RGB star member candidates from Section 4.1 both for metallicities and [C/Fe] abundances (see Table 2). We adopted the solar reference values from Asplund et al. (2009). The chemical abundances of the "unlikely members" of Tucana IV are listed in Table B.1 however, if they are not members, the adopted stellar parameters are probably not reliable.

5.1. Iron

We derive the [Fe/H] ratios using the second and third EWs of the Ca II triplet lines (8542 Å and 8662 Å) through the empirical relation of Starkenburg et al. (2010) (their Eq. 5). We use these lines because the S/N ratio is not sufficient to accurately measure the metallicity from the weak Fe lines in these metal-poor stars.

We convert our G Gaia magnitude to V Johnson-Cousin magnitude by using the following formula (Carrasco & Bellazzini 2020):

$$G_0 - V_0 = -0.02704 + 0.01424(BP - RP)_0 - 0.2156(BP - RP)_0^2 + 0.01426(BP - RP)_0^3$$

The synthetic spectrum of all Ca II triplet lines was created using Turbospectrum in a well-defined smaller wavelength range (as explained in Section 3.4). In this case, it was not possible to gain accurate fits with 1D LTE synthetic spectra with correct parameters due to non-local thermodynamic equilibrium (NLTE) effects, which affect the line profile in a way that is not reproduced with the LTE synthetic spectra, but can be mimicked by changing the input parameters. The EWs were then measured from the best fit synthetic spectrum, minimizing the χ^2 (Figure 8).

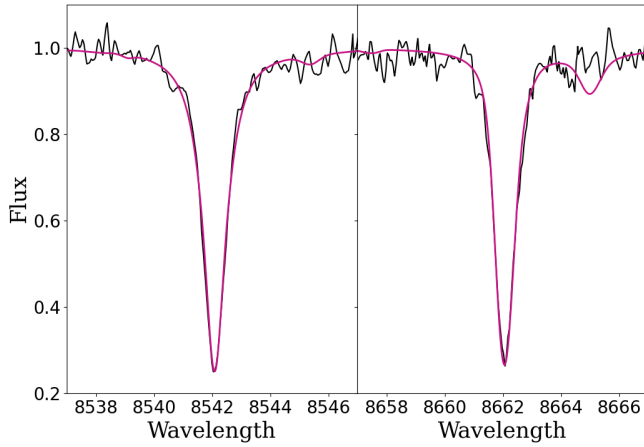


Fig. 8: Best fit of EW₂ (8542 Å) and EW₃ (8662 Å) of star 26 in Grus II. The black line is the observed spectrum, the magenta line is the synthetic spectrum.

Tolstoy et al. (2023) reports the ratio between the EWs of the second and third lines of the calcium triplet as a function of S/N for RGB stars in the Sculptor dSph galaxy. To verify that our results are not skewed in the limit of the lowest S/N, Figure 9 shows the comparison of our measured EW ratio, EW₂/EW₃, with their results. Since we have no measurements in the region beyond the region considered reasonable by Tolstoy et al. (2023), we infer that the EW ratios are constant with the S/N as expected, indicating that our results are not severely skewed in the limit of low S/N. In the right panel of Figure 9, we highlight the difference between the reddest Ca II triplet line (8662 Å) for a metal-poor and a metal-rich star.

Figure 10 shows the Metallicity Distribution Function (MDF) of the member stars in Grus II and Tucana IV. The MDF of Grus II is shifted towards lower metallicity than that of Tucana IV, leading to a higher probability of finding CEMP-no stars in the first galaxy since these stars are more common at low metallicity (e.g. Beers & Christlieb 2005; Salvadori et al. 2015). Because of the low number statistics (especially in Tucana IV), we do not draw any concrete conclusion about the star formation history.

Table 2: Chemical measurements of RGB member stars in Grus II and Tucana IV. [C/Fe] are the carbon abundances corrected using the Placco et al. (2014) tool.

Grus II					
star ID	[Fe/H]	$\sigma_{[\text{Fe}/\text{H}]}$	[C/Fe] ₀	[C/Fe]	$\sigma_{[\text{C}/\text{Fe}]}$
3	-2.93	0.25	0.00	0.01	0.33
4	-2.93	0.32	2.08	2.10	0.39
9	-2.92	0.51	1.30	1.31	0.57
13	-2.69	0.26	0.76	0.77	0.33
26	-2.76	0.24	-0.34	-0.10	0.33
29	-2.24	0.27	0.98	1.00	0.35
30	-2.88	0.26	1.36	1.37	0.34
122	-2.47	0.25	-0.78	-0.14	0.32

Tucana IV					
star ID	[Fe/H]	$\sigma_{[\text{Fe}/\text{H}]}$	[C/Fe] ₀	[C/Fe]	$\sigma_{[\text{C}/\text{Fe}]}$
5	-1.38	0.28	-0.70	-0.30	0.35
7	-2.75	0.26	0.82	0.83	0.33
8	-2.09	0.27	0.04	0.05	0.36

According to Starkenburg's formula, the errors on [Fe/H] are obtained with

$$\sigma_{[\text{Fe}/\text{H}]} = \sqrt{(0.195 + 0.0155EW_{2+3})^2 \sigma_{V-V_{\text{HB}}}^2 + (0.458 + 1.3695EW_{2+3}^{-2.5} + 0.0155(V - V_{\text{HB}}))^2 \sigma_{EW_{2+3}}^2 + \sigma_{\text{par}}^2} \quad (9)$$

where $\sigma_{EW_{2+3}}$ is the error on the sum of EW₂ and EW₃; $\sigma_{(V-V_{\text{HB}})}$ is the error on the mean of the V magnitude of HB stars, ($V_{\text{HB}}=19.14 \pm 0.14$ for Grus II and $V_{\text{HB}}=19.07 \pm 0.14$ for Tucana IV, derived by averaging the V magnitude of the HB stars in our sample); σ_{par} is the contribution derived from the fitted parameters, estimated to be 8% (Starkenburg et al. 2010). The error on the individual EWs is found by adopting the formula from Battaglia et al. (2008) (their Eq. 3) and then summed in quadrature. The [Fe/H] values of member stars and their respective errors are reported in Table 2. Moreover, we tested the impact of the systematic error due to the continuum level assuming different S/N, which results $\sigma_{[\text{Fe}/\text{H}],\text{sys}} \lesssim 0.05$.

We made a check for the brightest stars (5 in Tuc IV and 26 in Grus II) measuring the [Fe/H] with the Fe lines and the results are in agreement with the Ca triplet measurements.

5.2. Carbon

To measure the C abundances (Figure 1), we created a synthetic spectrum as described in Section 4.1, adopting the stellar parameters from Section 3 and [Fe/H] from Section 5.1. The synthetic spectrum is generated around the CH-band at 4300 Å in a wavelength range of 80 Å (Figure 11). We used the online tool developed by Placco et al. (2014) to correct the C abundances for the internal mixing occurring in the RGB stars.

Figure 12 shows the [C/Fe] relation as a function of [Fe/H]. In Grus II, we identify 3 CEMP stars (stars 4, 9, and 30) with [C/Fe] > +1 and 2 CEMP stars (stars 13 and 29) with [C/Fe] > +0.7 and slightly higher [Fe/H]. In Tucana IV, star 7

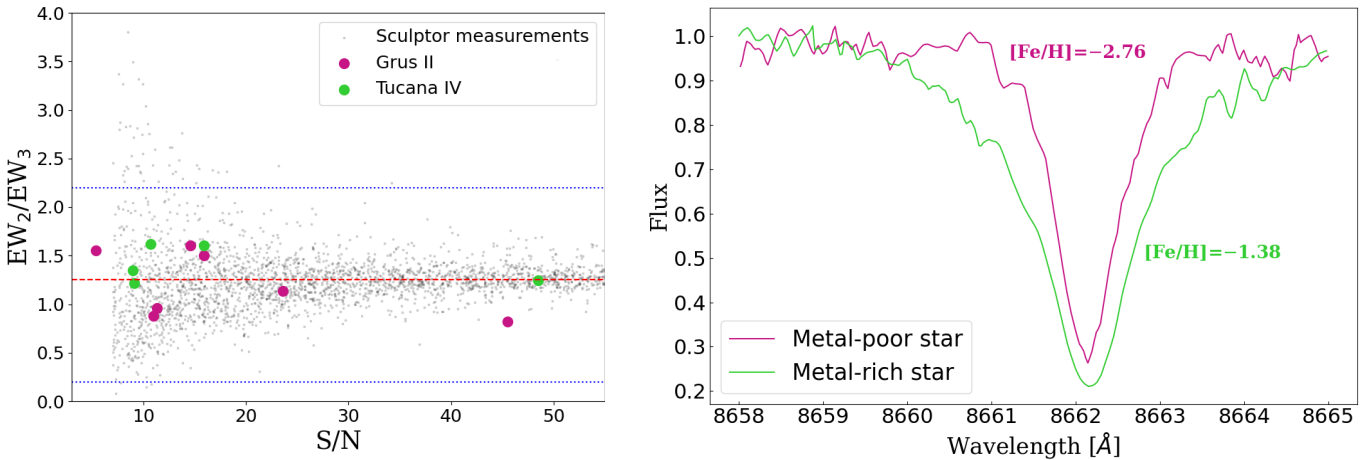


Fig. 9: **Left:** Ratios of the EWs of two Ca II lines (8542 Å and 8662 Å) as a function of S/N. The two horizontal blue lines are limits of $\text{EW2}/\text{EW3}$ at $0.2 < \text{EW2}/\text{EW3} < 2.2$, defined as reasonable values by Tolstoy et al. (2023). **Right:** Comparison between spectra of the metal-rich star 5 in Tucana IV and the metal-poor star 26 in Grus II.

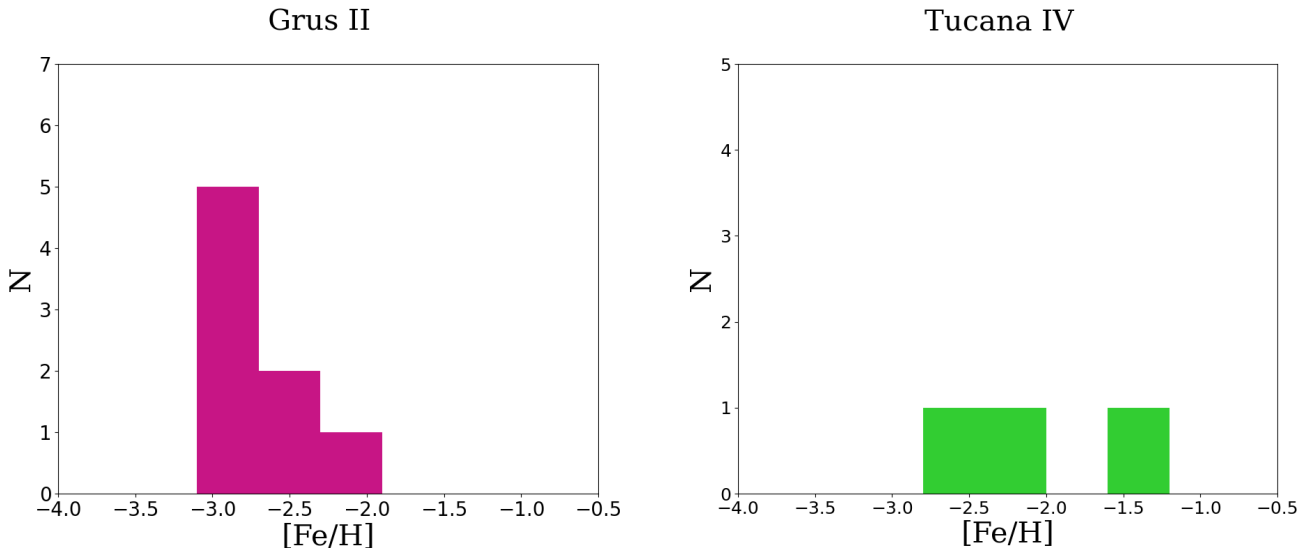


Fig. 10: Metallicity distribution functions. In Tucana IV, the "unlikely members" are not included in the distribution. The typical errors on the $[\text{Fe}/\text{H}]$ are 0.27.

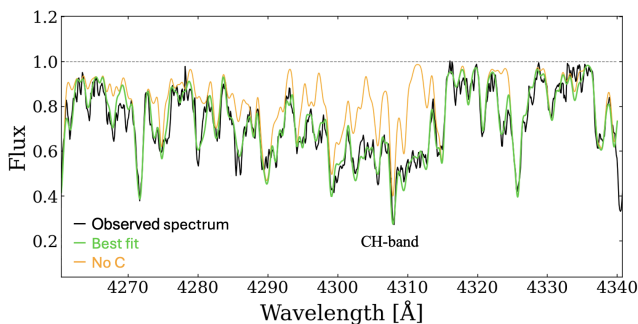


Fig. 11: Best fit of the CH band of the star 5 in Tucana IV. The black line is the observed spectrum, the green line is the synthetic spectrum.

has $[\text{C}/\text{Fe}] > +0.7$. All the C measurements are reported in Table 2.

For these CEMP stars we looked at the Ba II line at 4554 Å in LR2. However, since the line is at the edge of the spectrum and S/N is very low (Table E.1), we were only able to derive upper limits of the Ba abundances: in Grus II, stars 4 and 13 have $[\text{Ba}/\text{Fe}] \lesssim 0.6$, star 29 has $[\text{Ba}/\text{Fe}] \lesssim 0.2$ and stars 30 and 9 have $[\text{Ba}/\text{Fe}] \lesssim 0.7$. In Tucana IV star 7 has $[\text{Ba}/\text{Fe}] \lesssim 0.2$. Additionally, we derived the absolute abundances $A(\text{C})$ to verify the nature of these CEMP stars (Figure 12, right): we point out that the stars that fall in the high C-band (i.e. have an absolute C abundance close to the solar value), populate a region which is primarily occupied by CEMP-s stars (Bonifacio et al. 2015). Remembering that CEMP-s stars have $[\text{Ba}/\text{Fe}] > 1$ and high absolute C abundances, we can conclude that all the CEMP stars found in Grus II and star 7 in Tucana IV are CEMP-no stars. We note that technically these identified CEMP stars could possibly be CEMP-r stars since we do not have Eu measurements. However, this kind of CEMP stars are extremely rare and only a few have been identified in the Milky Way halo.

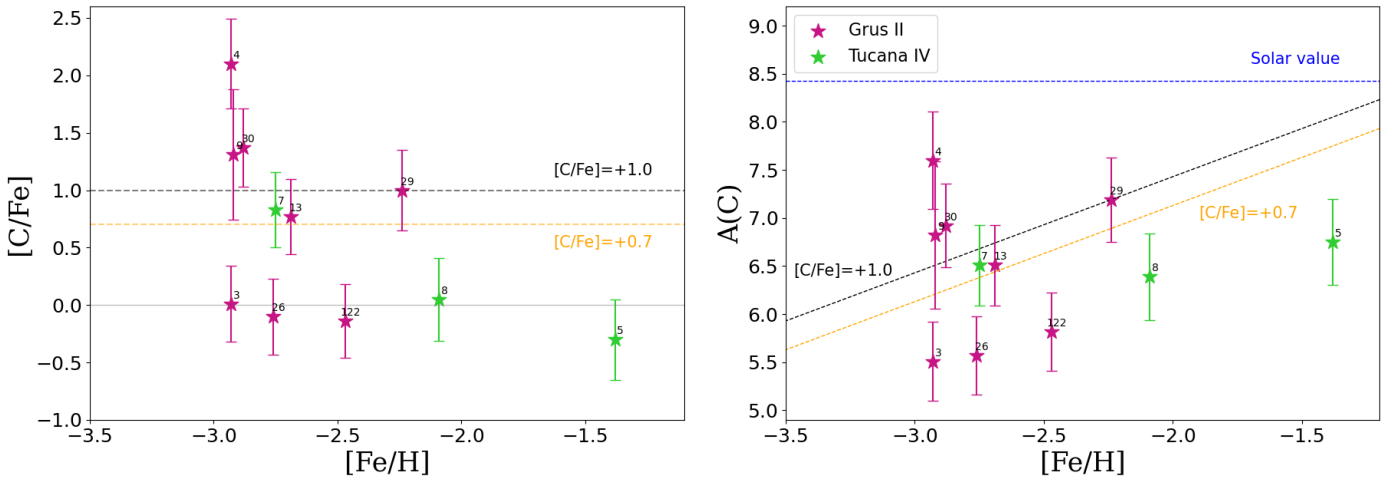


Fig. 12: Left: $[C/Fe]$ as a function of metallicity. The dashed orange line is $[C/Fe] = +0.7$, while the black dashed line is the other threshold commonly assumed in the literature for CEMP stars, $[C/Fe] = +1$. Right: The absolute C abundance as a function of $[Fe/H]$. The dashed blue line represents the solar value $A(C)_\odot = 8.43$ (Asplund et al. 2009).

All the abundances (Fe, C and Ba) were derived under the LTE assumption, allowing us to compare the abundances with other measurements present in the literature. The uncertainties on the C abundances consist of two contributions, which were added quadratically to obtain the total errors. The first is the random error which is found by deriving the $[C/Fe]$ in five different regions of 10 Å from 4270 Å to 4320 Å, covering the entire CH-band. We obtained the errors by calculating the standard deviation of these five $[C/Fe]$ measurements. For $S/N > 7$, $\sigma_{C,rand}$ is $\lesssim 0.1$ dex, while for $5 < S/N < 7$ $\sigma_{C,rand}$ is ~ 0.15 dex³. The second contribution is due to the stellar parameters and is dominated by the error on the T_{eff} , i.e. $\sigma_{C,T_{\text{eff}}} \sim 0.2$ dex. The total error on $[C/Fe]$ was found with the quadratic sum of both the errors on C and Fe abundances (see Table 2).

6. Comparison with literature

Both Grus II and Tucana IV have also been investigated by Simon et al. (2020). They observed stars in Grus II and Tucana IV with the IMACS spectrograph on the Magellan/Baade Telescope. Their spectra have $R=11\,000$, in a wavelength range from 7500 to 8900 Å. We checked the presence of stars in common between the two samples: there are 14 stars in Grus II and 9 stars in Tucana IV in common, allowing us to make a comparison between the results. The upper panels of Figure 13 show the comparison between the radial velocity distributions, while the number values are reported in Table E.4 and Table E.5. The darker grey bars are the members identified by Simon et al. (2020): our distributions are completely in agreement, corroborating our identification of the members. We recall that the systemic radial velocity we derived for Grus II is $v_{\text{sys}} = -106.5 \pm 1.4$ km s⁻¹, resulting in a small offset from the value reported by Simon et al. (2020), $v_{\text{sys}} = -110.0 \pm 0.5$ km s⁻¹. In the case of Tucana IV, the systemic radial velocity is $v_{\text{sys}} = 14.9 \pm 1.9$ km s⁻¹, considering only the certain members, in good agreement with the value from Simon et al. (2020), $v_{\text{sys}} = 15.9^{+1.8}_{-1.7}$ km s⁻¹.

³ We remind that the S/N was underestimated in the region of the CH-band because of the lack of continuum points available (see Section 2).

Additionally, we compare the metallicity distribution functions with those of (Simon et al. 2020). The $[Fe/H]$ measurements of stars in common are consistent within the errors, therefore, despite the low number of stars, the two distributions are in agreement (see the lower panels in Figure 13). Numerical values are reported in Table E.4 and Table E.5.

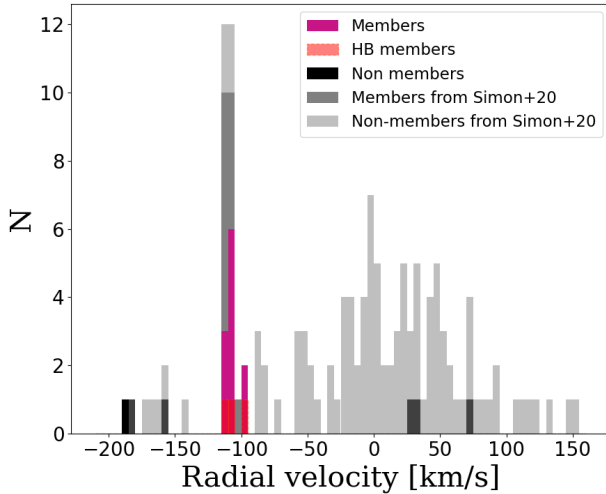
Finally, Hansen et al. (2020) analyzed the 3 brightest stars in Grus II (3, 26, 122) from a detailed chemical point of view, providing also the radial velocities (which are in agreement with our results). For the purpose of this work, our attention is focused on the C abundance. All the $[Fe/H]$ measurements and the $[C/Fe]$ of stars 26 and 122 are consistent, while star 3 has quite different $[C/Fe]$, but agrees on being a C-normal star (see Appendix D). Nevertheless, it is not a CEMP star, as we confirm with our abundance derivation.

7. Discussion and conclusions

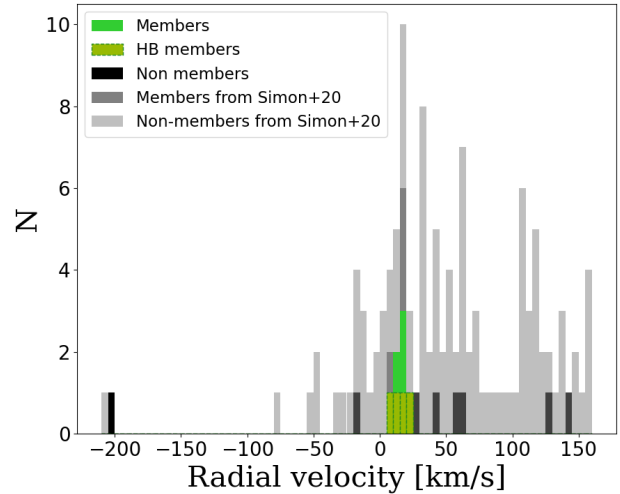
The aim of this work is to analyze the spectra of stars that belong to two ultra-faint dwarf galaxies, Grus II and Tucana IV, and derive the carbon abundance in RGB members. In particular, we focused on identifying the CEMP-no stars, whose chemical abundances are consistent with the imprint of primordial low-energy supernovae ($E \lesssim 10^{51}$ erg).

We derived the radial velocity of RGB and HB stars (Figure 4) using the Ca II triplet from the FLAMES/Giraffe HR21 spectra and hence determined the membership of the stars to the galaxies by combining our results with Gaia data. Moreover, we compared our results by checking the membership probability reported in Battaglia et al. (2022) based on Gaia eDR3 (Figure 5), where all of our identified members of Grus II have a membership probability higher than 80%. We note that 2 of the 13 Grus II members (stars 1 and 14) are HB stars with only LR2 spectra available, therefore they are not present in the figures and the consequent analysis. In Tucana IV there are 7 members with a probability over 80%. Afterward, we derived the metallicity distribution functions of the galaxies after an accurate determination of the EWs of the Ca II triplet. Tucana IV is shifted to higher metallicity than Grus II (Figure 10), therefore the probability of finding CEMP stars is lower.

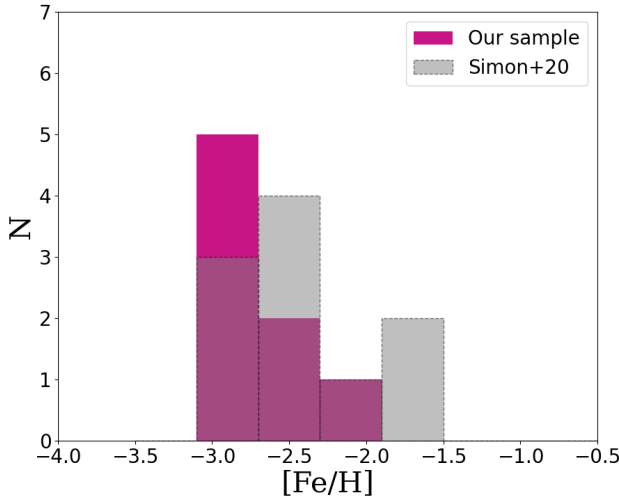
Grus II



Tucana IV



Grus II



Tucana IV

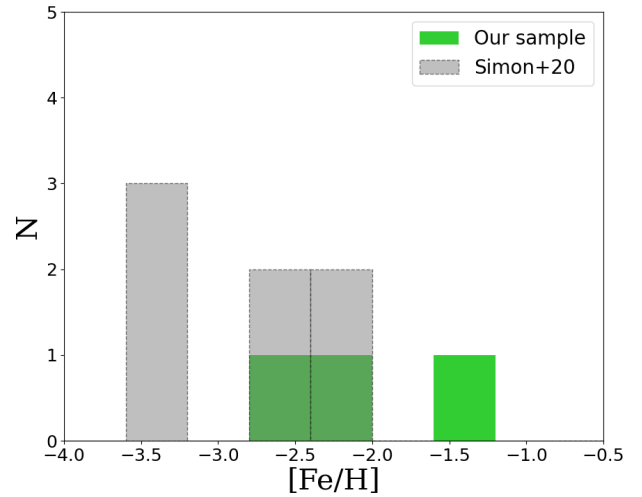


Fig. 13: Our radial velocity distributions (upper panels) and metallicity distribution functions (lower panels) compared with [Simon et al. \(2020\)](#).

Finally, we derived the [C/Fe] to identify carbon-rich stars ([Figure 12](#)): 5 CEMP-no stars (thereof 3 with [C/Fe] > +1) were found in Grus II, while in Tucana IV we discovered one CEMP-no star. The categorization into CEMP-no stars was based on A(C) and upper limits on Ba (Section 5.2), but further investigation is needed to obtain reliable Ba measurements. Among our identified members in Grus II and Tucana IV, 10 stars are very metal-poor ([Fe/H] < -2), thereof 6 CEMP-no stars with [C/Fe] > +0.7. According to [Ji et al. \(2020b\)](#), the fraction of CEMP stars at such metallicity is $21 \pm 5\%$. In our case this fraction is $60^{+36\%}_{-24\%}$ ([Gehrels 1986](#)), therefore in these two UFDs the fraction of CEMP-no stars is higher than the average. Considering the threshold of [C/Fe] > +1, we found 3 CEMP-no stars, therefore $30^{+29\%}_{-16\%}$ ([Gehrels 1986](#)) which is in agreement with [Ji et al. \(2020a\)](#) results, i.e. $\approx 10 \pm 5\%$ (assuming similar errors as for [C/Fe] > +0.7). We can conclude that in Grus II and Tucana IV, faint Pop III SNe likely exploded, enhancing the ISM with high [C/Fe] and maintaining this peculiar abundance ratio in the photosphere of the second-generation stars. However, in the case of Grus II (where we found 5 CEMP-no stars), we cannot conclude if these stars derived from the same first faint SN or if several such events occur even in this small galaxy

($M_* = 3.4^{+0.3}_{-0.4} \times 10^3 M_\odot$). Combining this data analysis with literature data could be potentially useful to constrain and understand the star formation history in these small systems.

Even though the UFDs are among the nearest galaxies where it is possible to detect single stars, obtaining spectra of stars in these systems is challenging. This is why there are very few chemical measurements of the populations of these systems in the literature, contained in two principal catalogs, SAGA ([Suda et al. 2008](#)) and JINA ([Abohalima & Frebel 2018](#)). In the SAGA database which contains the most complete compilation of literature C measurements in metal-poor stars, there are only 78 measurements of carbon abundances in UFDs. By only analyzing a few RGB stars in Grus II and Tucana IV, we improve this number by $\sim 14\%$. This allows us to better understand the CEMP fraction in the UFDs and the imprint that the first stars had in such pristine and ancient systems.

Acknowledgements.

This project has received funding from the European Research Council (ERC) under the European Union’s Horizon 2020 research and innovation programme (grant agreement No. 101117455). J. M. Arroyo acknowledges support from the Agencia Estatal de Investigación del Ministerio de Ciencia en Innovación (AEI-MICIN) and the European Social Fund (ESF+) under grant PRE2021-100638. J. M. Arroyo and G. Battaglia acknowledge support from the Agen-

cia Estatal de Investigación del Ministerio de Ciencia, Innovación y Universidades (MCIU/AEI) under grant "En La Frontera De La Arqueología Galáctica: Evolución De La Materia Luminosa Y Oscura De La Vía Láctea Y Las Galaxias Enanas Del Grupo Local En La Era De Gaia. (FOGALERA)" and the European Regional Development Fund (ERDF) with reference PID2023-150319NB-C21/10.13039/501100011033. A.Mucciarelli, acknowledges support from the project "LEGO – Reconstructing the building blocks of the Galaxy by chemical tagging" (P.I. A. Mucciarelli) granted by the Italian MUR through contract PRIN 2022LLP8TK_001. D.Massari acknowledges financial support from PRIN-MIUR-22: CHRONOS: adjusting the clock(s) to unveil the CHRONO-chemo-dynamical Structure of the Galaxy" (PI: S. Cassisi), and from the INAF Mini Grant 2023 (Ob.Fu. 1.05.23.04.02 – CUP C33C23000960005) CHAM – Chemo-dynamics of the Accreted Halo of the Milky Way (P.I.: M. Bellazzini). We thank J. Simon for useful discussion and insightful suggestions.

References

Abohalima, A. & Frebel, A. 2018, *ApJS*, 238, 36

Andrae, R., Fouesneau, M., Creevey, O., et al. 2018, *A&A*, 616, A8

Anthony-Twarog, B. J., Delfiannis, C. P., Rich, E., & Twarog, B. A. 2013, *ApJ*, 767, L19

Aoki, W., Beers, T. C., Christlieb, N., et al. 2007, *ApJ*, 655, 492

Asplund, M., Grevesse, N., Sauval, A. J., & Scott, P. 2009, *Annual Review of Astronomy and Astrophysics*, 47, 481

Battaglia, G., Irwin, M., Tolstoy, E., et al. 2008, *MNRAS*, 383, 183

Battaglia, G., Taibi, S., Thomas, G. F., & Fritz, T. K. 2022, *A&A*, 657, A54

Beers, T. C. & Christlieb, N. 2005, *ARA&A*, 43, 531

Bonifacio, P., Caffau, E., Spite, M., et al. 2015, *A&A*, 579, A28

Bovill, M. S. & Ricotti, M. 2009, *ApJ*, 693, 1859

Bressan, A., Marigo, P., Girardi, L., et al. 2012, *MNRAS*, 427, 127

Bromm, V. & Yoshida, N. 2011, *ARA&A*, 49, 373

Brown, T. M., Tumlinson, J., Geha, M., et al. 2014, *ApJ*, 796, 91

Carrasco, J. M. & Bellazzini, M. 2020, 5.5.1 Relationships with other photometric systems, <https://gea.esac.esa.int/archive/documentation/GEDR3/>, gaia EDR3 Documentation, ESA

Carretta, E., Bragaglia, A., Gratton, R. G., & Tosi, M. 2004, *A&A*, 422, 951

Chiti, A., Placco, V. M., Pace, A. B., et al. 2025, arXiv e-prints, arXiv:2508.04053

Chiti, A., Simon, J. D., Frebel, A., et al. 2018, *ApJ*, 856, 142

Drlica-Wagner, A., Bechtol, K., Rykoff, E. S., et al. 2015, *ApJ*, 813, 109

Frebel, A. & Bromm, V. 2012, *ApJ*, 759, 115

Frebel, A., Kirby, E. N., & Simon, J. D. 2010, *Nature*, 464, 72

Gaia Collaboration, Babusiaux, C., Van Leeuwen, F., et al. 2018, *A&A*, 616, A10

Gallart, C., Monelli, M., Ruiz-Lara, T., et al. 2021, *ApJ*, 909, 192

Gehrels, N. 1986, *ApJ*, 303, 336

Gustafsson, B., Edvardsson, B., Eriksson, K., et al. 2008, *A&A*, 486, 951

Hansen, T. T., Andersen, J., Nordström, B., et al. 2015, *A&A*, 583, A49

Hansen, T. T., Marshall, J. L., Simon, J. D., et al. 2020, *ApJ*, 897, 183

Hansen, T. T., Simon, J. D., Li, T. S., et al. 2024, *ApJ*, 968, 21

Hartwig, T. & Yoshida, N. 2019, *ApJ*, 870, L3

Hirano, S., Hosokawa, T., Yoshida, N., et al. 2014, *ApJ*, 781, 60

Iwamoto, N., Umeda, H., Tominaga, N., Nomoto, K., & Maeda, K. 2005, *Science*, 309, 451

Jablonka, P., North, P., Mashonkina, L., et al. 2015, *A&A*, 583, A67

Jenkins, S. A., Li, T. S., Pace, A. B., et al. 2021, *ApJ*, 920, 92

Jeon, M., Bromm, V., Besla, G., Yoon, J., & Choi, Y. 2021, *MNRAS*, 502, 1

Ji, A. P., Li, T. S., Simon, J. D., et al. 2020a, *ApJ*, 889, 27

Ji, A. P., Li, T. S., Simon, J. D., et al. 2020b, *ApJ*, 889, 27

Koch, A., Hansen, T., Feltzing, S., & Wilkinson, M. I. 2014, *ApJ*, 780, 91

Komiya, Y., Suda, T., Yamada, S., & Fujimoto, M. Y. 2020, *ApJ*, 890, 66

Lee, Y. S., Beers, T. C., Masseron, T., et al. 2013, *AJ*, 146, 132

Lucchesi, R., Jablonka, P., Skúladóttir, Á., et al. 2024, *A&A*, 686, A266

Martínez-Vázquez, C. E., Vivas, A. K., Gurevich, M., et al. 2019, *MNRAS*, 490, 2183

Massari, D. & Helmi, A. 2018, *A&A*, 620, A155

McConnachie, A. W. 2012, *The Astronomical Journal*, 144, 4

Mucciarelli, A. & Bellazzini, M. 2020, *Research Notes of the AAS*, 4, 52

Mucciarelli, A., Bellazzini, M., & Massari, D. 2021, *A&A*, 653, A90

Norris, J. E., Wyse, R. F. G., Gilmore, G., et al. 2010, *ApJ*, 723, 1632

Norris, J. E., Yong, D., Bessell, M. S., et al. 2013, *ApJ*, 762, 28

Pace, A. B. & Li, T. S. 2019, *ApJ*, 875, 77

Placco, V. M., Frebel, A., Beers, T. C., & Stancliffe, R. J. 2014, *ApJ*, 797, 21

Plez, B. 2012, *Turbospectrum: Code for spectral synthesis, Astrophysics Source Code Library*, record ascl:1205.004

Rossi, M., Salvadori, S., & Skúladóttir, Á. 2021, *MNRAS*, 503, 6026

Rossi, M., Salvadori, S., Skúladóttir, Á., Vanni, I., & Koutsouridou, I. 2024, *Hidden Population III Descendants in Ultra-Faint Dwarf Galaxies*, arXiv:2406.12960 [astro-ph]

Salvadori, S. & Ferrara, A. 2009, *Monthly Notices of the Royal Astronomical Society: Letters*, 395, L6

Salvadori, S., Skúladóttir, Á., & Tolstoy, E. 2015, *Monthly Notices of the Royal Astronomical Society*, 454, 1320

Simon, J. D. 2019, *ARA&A*, 57, 375

Simon, J. D., Jacobson, H. R., Frebel, A., et al. 2015, *ApJ*, 802, 93

Simon, J. D., Li, T. S., Erkal, D., et al. 2020, *ApJ*, 892, 137, arXiv:1911.08493 [astro-ph]

Skúladóttir, Á., Salvadori, S., Amarsi, A. M., et al. 2021, *ApJ*, 915, L30

Skúladóttir, Á., Tolstoy, E., Salvadori, S., et al. 2015, *Astronomy & Astrophysics*, 574, A129

Skúladóttir, Á., Vanni, I., Salvadori, S., & Lucchesi, R. 2024, *A&A*, 681, A44

Starkenburg, E., Hill, V., Tolstoy, E., et al. 2013, *A&A*, 549, A88

Starkenburg, E., Hill, V., Tolstoy, E., et al. 2010, *Astronomy and Astrophysics*, 513, A34

Starkenburg, E., Shetrone, M. D., McConnachie, A. W., & Venn, K. A. 2014, *MNRAS*, 441, 1217

Suda, T., Katsuta, Y., Yamada, S., et al. 2008, *PASJ*, 60, 1159

Susmitha, A., Koch, A., & Sivarani, T. 2017, *A&A*, 606, A112

Tafelmeyer, M., Jablonka, P., Hill, V., et al. 2010, *A&A*, 524, A58

Tegmark, M., Silk, J., Rees, M. J., et al. 1997, *ApJ*, 474, 1

Tolstoy, E., Skúladóttir, Á., Battaglia, G., et al. 2023, *A&A*, 675, A49

Appendix A: Isochrones

Figure A.1 shows the CMD with isochrones from PARSEC tool (Bressan et al. 2012) plotted for different metallicity. We note that below $G < 20$ we reach the limit of Gaia, so a spread in photometry is expected because of large uncertainties and our data are not deep enough to reach the main sequence turn-off. The HB of our data agrees with the isochrones, showing that we are in agreement with the distances estimated in Drlica-Wagner et al. (2015).

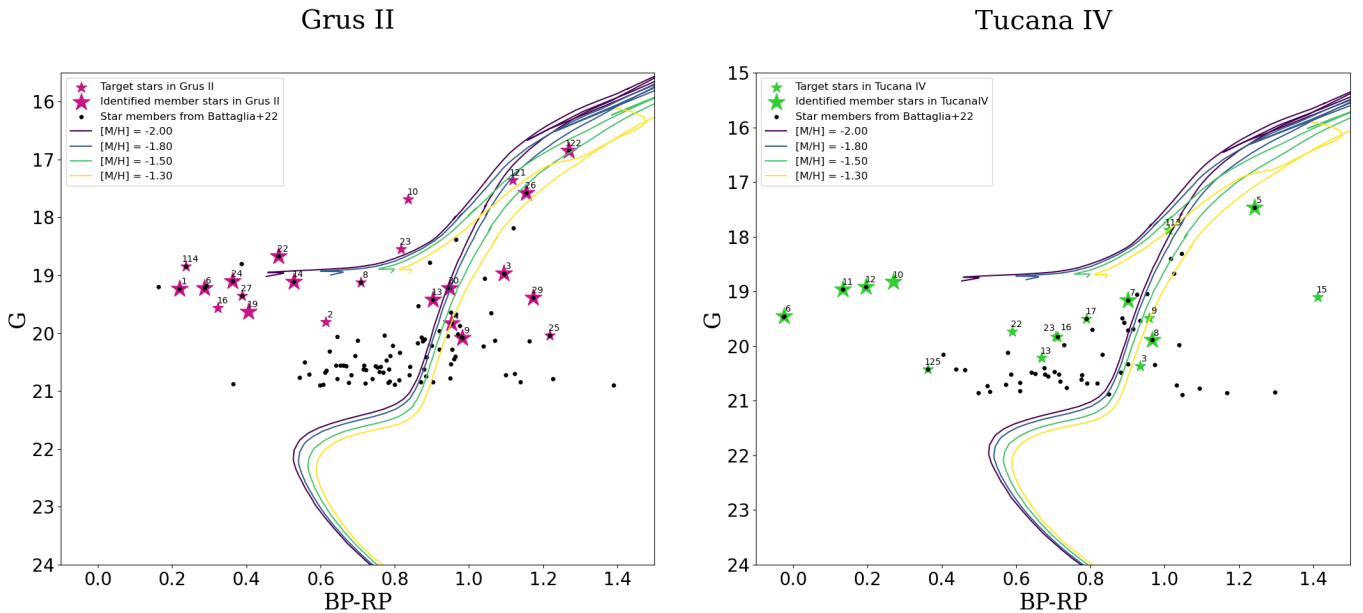


Fig. A.1: Color-magnitude diagram with isochrones. Our stars fall on the RGB and HB.

Appendix B: Radial velocity analysis of near-peak stars in Tucana IV

Table B.1: Radial velocity and chemical abundances of the stars 9, 16, 17, 22 and 113 in Tucana IV.

star ID	v_{rad} [km s $^{-1}$]	$e_{v_{\text{rad}}}$ [km s $^{-1}$]	Tucana IV				
			[Fe/H]	$\sigma_{[\text{Fe}/\text{H}]}$	$[\text{C}/\text{Fe}]_0$	[C/Fe]	$\sigma_{[\text{C}/\text{Fe}]}$
9	29.3	1.3	-1.28	0.29	-0.12	-0.10	0.36
16	-18.1	1.7	-2.46	0.28	0.68	0.69	0.59
17	59.3	1.7	-2.32	0.29	0.83	1.00	0.38
22	60.3	1.7	-1.86	0.28	1.70	1.71	0.38
113	43.5	0.4	-1.48	0.28	-0.05	0.05	0.35

Stars 9, 16, 17, 22 and 113 in Tucana IV are classified as "unlikely members" according to radial velocity determination (Section 4.1) and Gaia parameters (proper motions, parallax and position on CMD). However, we performed the chemical abundance analysis described in Section 5 also for these stars and the results are reported in Table B.1.

We derived different radial velocities of star 16 from exposures obtained in different epochs (-19.2 km s $^{-1}$ and -16.7 km s $^{-1}$), which suggests a possible binary star. However, the deviation from the mean velocity of the galaxy is large so its semi-amplitude would be larger than that of binary systems already identified in dwarf galaxies (Koch et al. 2014; Hansen et al. 2024), making this star an unlikely member of Tucana IV. Star 22 is a possible CEMP-s star (i.e. likely a binary star, see Section 5.2) which can explain its deviation from the central peak. However, without certain [Ba/Fe] abundance measurements, we cannot confirm its nature. Moreover, the semi-amplitude would be too large for the star to be a Tucana IV member (as in the case of star 16). Stars 17 and 113 have acceptable proper motions and parallax, but we do not see any evidence of binarity due in part to having only two epochs. Star 9 differs $5\sigma_{pm}$ from the systemic proper motion of Tucana IV (see Figure 5). Here, σ_{pm} denotes the total dispersion of the proper motions distribution.

Stars 16, 17 and 22 have [C/Fe] consistent with the threshold for CEMP classification. In particular, star 22 has $[\text{Ba}/\text{Fe}] \lesssim 1.5$ and falls in the high-C band, therefore could be classified as a possible CEMP-s star. However, we note that should any of these stars be non-members at very different distances compared to the galaxies, the derived stellar abundances, and hence also their chemical abundance measurements, cannot be considered reliable.

Appendix C: Radial velocity in blue

Figure C.1 shows the difference between the radial velocities measured from the HR21 and LR2 spectra. The solid line is the mean of the difference, while the dashed lines are $\pm 1\sigma$ from the mean. We note that the zero-point in the blue could not be verified because of the lack of skylines, therefore the errors do not include a possible systematic offset. Stars 22 in Grus II and 12 in Tucana IV are HB stars and have very different radial velocities between red and blue. However, we remember that the blue spectra present very broad molecular features, lower S/N and resolution that make the radial velocity measurements less trustworthy than the ones from the Ca II triplet (see Section 4.1). For these stars, we also obtained the radial velocities from the two epochs available: for star 22 in Grus II we found $\Delta v = 10 \text{ km s}^{-1}$ and for star 12 in Tucana IV $\Delta v = 2.5 \text{ km s}^{-1}$, indicating that the hypothesis of binaries could not be excluded. In particular, star 22 in Grus II is a special case, since the Ca triplet lines are completely contaminated by the skylines as we explained in Section 4.1. Moreover, we note that this star corresponds to the variable star V2 studied in Martínez-Vázquez et al. (2019), who conclude that this is more likely to be a member of the Orphan-Chenab stellar stream. Thus, the radial velocity variation detected in star 22 in our Grus II sample is likely caused by pulsations.

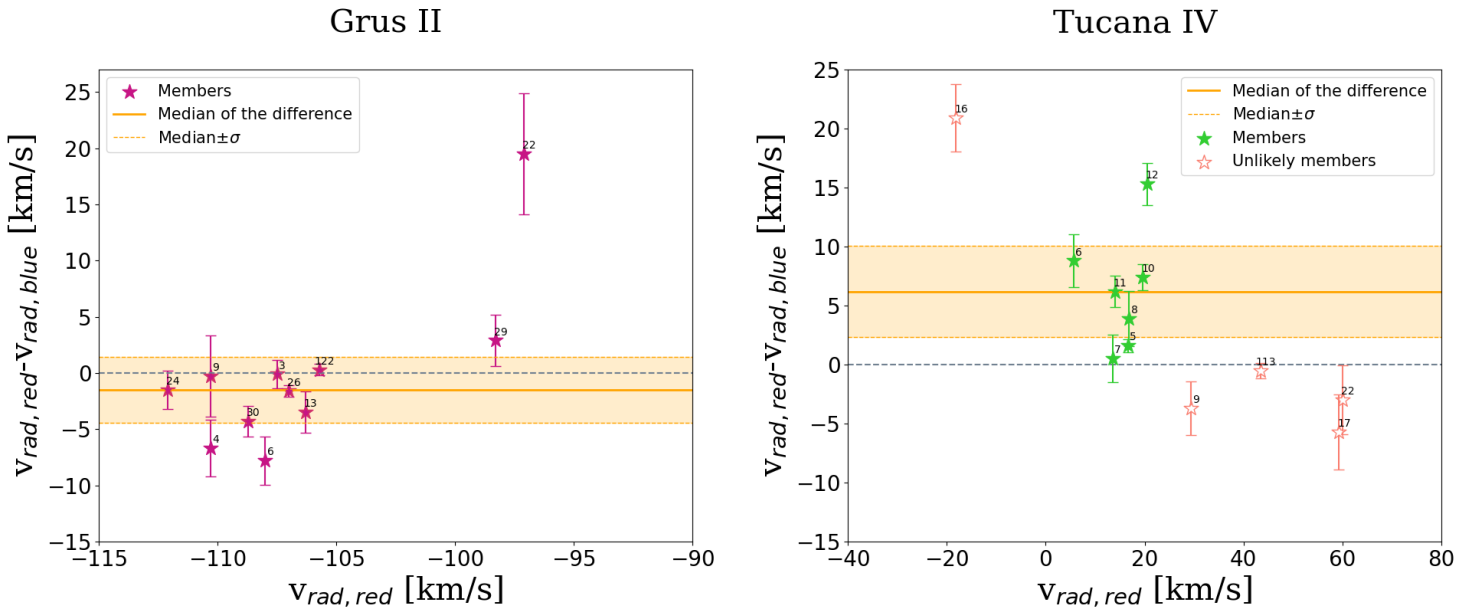


Fig. C.1: Difference of radial velocity measurements in the red and the blue. The solid line is the mean of the difference, the shaded areas cover $\pm 1\sigma$ from the mean. **Left:** star 22 shows a big offset which can indicate a possible binary nature and/or be a sign of pulsations. **Right:** stars 9, 16, 17, 22 and 113 are classified as "unlikely members" as explained in Section 4.2.

Appendix D: Comparison with literature results

In Table D.1 are listed the three stars in Grus II in common with Hansen et al. (2020). The radial velocities are in agreement within the errors for all the stars. Moreover, the metallicities and carbon abundances are consistent with Hansen et al. (2020) within the errors.

Table D.1: Comparison with (Hansen et al. 2020) for the three stars in common. The [C/Fe] and A(C) values reported are not corrected for the internal mixing.

star ID	T_{eff} [K]	$T_{\text{eff,Hansen}}$ [K]	$\log g_*$	$\log g_{*,\text{Hansen}}$	v_{rad} [km s $^{-1}$]	$v_{\text{rad,Hansen}}$ [km s $^{-1}$]	[Fe/H]	[Fe/H] _{Hansen}	[C/Fe]	[C/Fe] _{Hansen}	A(C)	A(C) _{Hansen}
3	4944	5121	2.27	1.91	-107.5	-106.5	-2.93	-2.94	0.00	+0.52	5.50	6.01
26	4823	4740	1.66	1.55	-107.0	-106.6	-2.76	-2.69	-0.34	-0.33	5.33	5.41
122	4614	4556	1.27	1.22	-105.7	-106.9	-2.47	-2.49	-0.78	-0.72	5.18	5.22

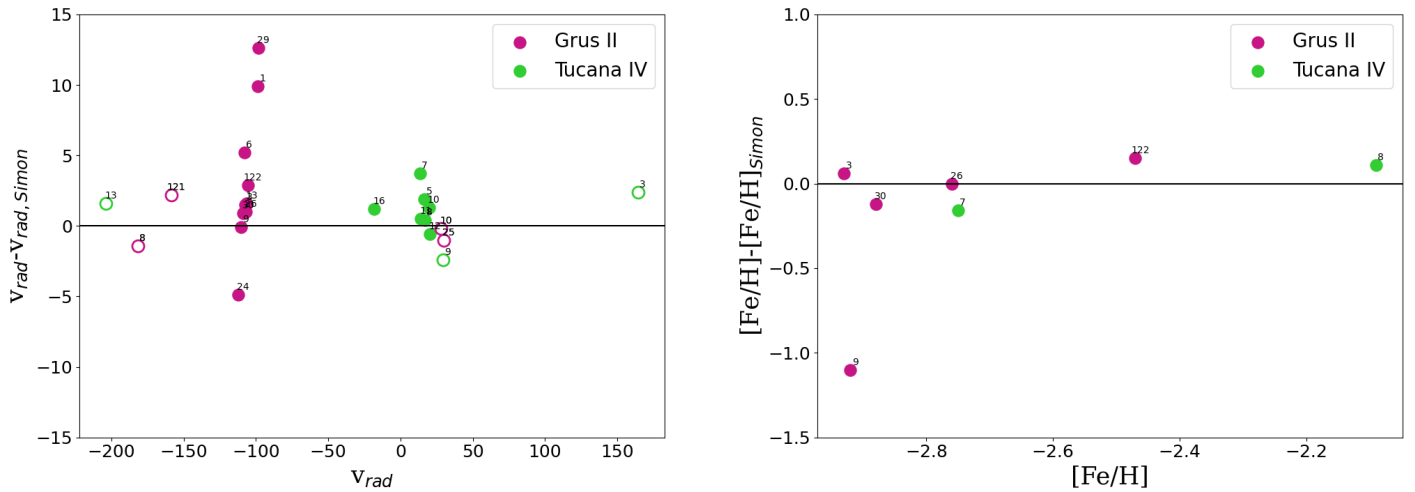


Fig. D.1: Comparison between our and Simon et al. (2020) results in radial velocity (left) and [Fe/H] (right). The empty symbols are the non-member stars.

Appendix E: Additional Tables

Table E.1: The number of exposures in HR21 and LR2 settings with the corresponding S/N per pixel values, and radial velocities from the Ca triplet with corresponding uncertainties. The italic ID identifies the stars whose radial velocities are derived from the blue spectra, while the “*” symbol represents the HB stars. We note that stars 14 and 22 in Grus II correspond to variable stars V1 and V2 studied in Martínez-Vázquez et al. (2019). They concluded that star 14 (their V1) is a Grus II member, but HB star 22 (their V2) is more likely to be a member of the Orphan-Chenab stellar stream.

Grus II						
star ID	HR21	LR2	[S/N] _{HR21} pix ⁻¹	[S/N] _{LR2} pix ⁻¹	v_{rad} [km s ⁻¹]	$e_{v_{\text{rad}}}$ [km s ⁻¹]
<i>1</i> *	—	2	—	21	-98.8	0.6
3	2	4	24	12	-107.5	0.5
4	2	2	11	7	-110.3	1.2
<i>6</i> *	2	2	7	20	-108.0	1.8
8	2	2	15	6	-181.9	0.8
9	4	4	5	6	-110.3	2.5
10	2	2	37	14	28.2	0.3
13	2	2	15	10	-106.3	0.9
<i>14</i> *	—	2	—	12	-104.0	1.1
<i>16</i> *	4	4	7	11	-189.7	2.0
<i>22</i> *	2	2	11	21	-97.1	1.1
23	2	2	24	4	74.9	0.5
<i>24</i> *	2	2	10	15	-112.1	1.3
25	4	4	13	2	30.1	1.0
26	2	2	46	22	-107.0	0.3
<i>27</i> *	2	2	7	13	171.1	1.7
29	2	2	11	8	-98.3	1.1
30	2	2	16	12	-108.7	0.8
<i>114</i> *	—	2	—	8	-22.4	1.6
121	2	2	52	26	-158.6	0.2
122	2	2	71	19	-105.7	0.2

Tucana IV						
star ID	HR21	LR2	[S/N] _{HR21} pix ⁻¹	[S/N] _{LR2} pix ⁻¹	v_{rad} [km s ⁻¹]	$e_{v_{\text{rad}}}$ [km s ⁻¹]
3	4	4	7	3	164.4	1.7
5	4	4	49	20	16.6	0.2
<i>6</i> *	4	4	7	15	5.6	1.8
7	4	4	16	8	13.5	0.8
8	4	4	11	8	16.9	1.2
9	4	4	11	8	29.3	1.1
<i>10</i> *	4	4	13	21	19.6	0.9
<i>11</i> *	4	4	11	21	14.0	1.2
<i>12</i> *	4	4	10	13	20.5	1.3
13	4	4	9	5	-203.8	1.5
15	4	4	12	2	143.3	1.0
16	4	4	9	6	-18.1	1.4
17	4	4	9	5	59.3	1.4
22	4	4	9	6	60.3	1.4
23	4	4	8	4	125.3	1.6
<i>113</i>	4	4	26	20	43.5	0.5
<i>125</i> *	—	4	—	6	-40.0	2.2

Table E.2. Stellar parameters and Gaia DR3 data for Grus II.

Gaia ID	star ID	RA	DEC	G	BP	RP	(BP - RP) ₀	(BP - G) ₀	(G - RP) ₀	μ_{α} [mas/yr]	μ_{δ} [mas/yr]	T _{eff} [K]	$\sigma_{T_{\text{eff}}}$ [K]	log g _*	V _{urb} [km s ⁻¹]
6561433598368152192	1	331.08387	-46.39487	19.2333	19.3114	19.0916	0.1919	0.0679	0.1240	0.273	-1.624	>6500	140	3.20	1.36
6561421778618145792	2	330.92058	-46.40760	19.8028	20.0295	19.4149	0.5913	0.2166	0.3748	0.069	-0.051	6146	80	3.04	1.39
6561421645474640000	3	330.96673	-46.41297	18.9611	19.4572	18.3629	1.0722	0.4846	0.5876	0.207	-1.782	4944	106	2.27	1.55
6561410199386304384	4	331.01845	-46.42266	19.8327	20.2353	19.2832	0.9289	0.3910	0.5379	0.127	-2.107	5238	87	2.75	1.45
6561432464496743296	6	331.14065	-46.44445	19.2171	19.3320	19.0454	0.2595	0.1047	0.1548	0.493	-1.445	>6500	162	3.12	1.38
6561419270357129856	8	330.88169	-46.53853	19.1157	19.4518	18.7424	0.6875	0.3262	0.3614	-0.155	-1.264	5853	202	2.68	1.46
6561433804526599168	9	331.06859	-46.37375	20.0840	20.5170	19.5352	0.9578	0.4209	0.5368	0.606	-2.154	5178	105	2.82	1.44
6561414498649007488	10	330.80891	-46.51693	17.6815	18.0132	17.1767	0.8161	0.3221	0.4940	-0.258	-2.036	5507	80	1.99	1.60
656140827935319926	13	331.07562	-46.54788	19.4178	19.7541	18.8516	0.8813	0.3260	0.5553	0.239	-1.310	5349	94	2.63	1.47
6561426485901552640	14	330.87292	-46.28101	19.1054	19.3193	18.7921	0.5029	0.2036	0.2993	0.496	-1.527	6430	126	2.84	1.43
6561434594800593024	16	331.21856	-46.35556	19.5657	19.7328	19.4089	0.3000	0.1580	0.1420	-0.442	-2.874	>6500	285	3.22	1.36
6561404633108542976	19	331.21860	-46.58282	19.6297	19.8025	19.3969	0.3802	0.1627	0.2175	-0.149	-0.166	6878	172	3.17	1.37
6561409409112267264	22	331.02493	-46.48206	18.6689	18.8711	18.3852	0.4628	0.1926	0.2702	0.318	-1.702	6569	147	2.71	1.46
6561436072268568064	23	331.10737	-46.25574	18.5485	18.8842	18.0676	0.7960	0.3259	0.4700	-120	-1.028	5557	92	2.35	1.53
6561420163710392704	24	330.92204	-46.46660	19.1005	19.2505	18.8884	0.3387	0.1409	0.1979	0.631	-1.467	>6500	163	3.00	1.40
6561445830435058816	25	331.03710	-46.32437	20.0408	20.5159	19.2976	1.1964	0.4632	0.7333	0.386	-1.749	4695	116	2.59	1.48
6561445628572018944	26	331.04160	-46.35068	17.5749	18.0758	16.9214	1.1316	0.4887	0.6429	0.421	-1.434	4823	81	1.66	1.67
656140727880404096	27	330.99326	-46.57928	19.3498	19.4765	19.0874	0.3651	0.1173	0.2478	0.353	-2.28	6968	83	3.08	1.38
6561410199386302592	29	331.00051	-46.42478	19.3876	19.9808	18.8078	1.1511	0.5814	0.5697	0.355	-1.380	4823	178	2.39	1.52
6561421572459692416	30	330.90051	-46.43441	19.2148	19.6126	18.6647	0.9256	0.3867	0.5388	0.442	-1.645	5246	86	2.50	1.50
6561431949.00750592	114	331.30712	-46.33453	18.8423	18.9432	18.7062	0.2155	0.0930	0.1226	0.584	-948	>6500	191	3.02	1.40
6561433305290770752	121	331.17323	-46.37917	17.3589	17.8510	16.7322	1.0960	0.4801	0.6159	0.360	-2.111	4892	88	1.61	1.68
6561403567956557312	122	331.09963	-46.61741	16.83500	17.4057	16.1368	1.2486	0.5444	0.7043	0.414	-2.111	4614	79	1.27	1.75

Table E.3: Stellar parameters and Gaia DR3 data for Tucana IV.

Gaia ID	star ID	RA	DEC	G	BP	RP	(BP – RP) ₀	(BP – G) ₀	(G – RP) ₀	μ_{α} [mas/yr]	μ_{δ} [mas/yr]	T _{eff} [K]	$\sigma_{T_{\text{eff}}}$ [K]	$\log g_{*}$	v_{turb} [km s ⁻¹]
4905854582002922112	3	0.71819	-60.73536	20.3699	20.8233	19.8899	0.9151	0.4443	0.4708	1.712	-3.205	5286	185	3.07	1.39
4905842693533910912	5	0.79783	-60.74766	17.4662	18.0192	16.7768	1.2245	0.5430	0.6815	0.519	-1.755	4658	82	1.63	1.67
4905854066606832640	6	0.60930	-60.77164	19.4535	19.4474	19.4719	-0.0445	-0.0125	-0.0321	0.259	-1.873	>6500	259	3.53	1.29
4905842212497084288	7	0.71638	-60.80579	19.1620	19.5857	18.6837	0.8845	0.4151	0.4694	0.546	-1.515	5351	163	2.61	1.48
4905838158047933056	8	0.73765	-60.86140	19.8914	20.2882	19.3216	0.9498	0.3884	0.5614	1.180	-1.158	5190	80	2.84	1.43
4905847984933119104	9	0.43461	-60.83191	19.4876	19.8772	18.9187	0.9433	0.3820	0.5613	2.013	-2.812	5205	79	2.69	1.46
4905841147345181568	10	0.76487	-60.84038	18.8278	18.9470	18.6767	0.2507	0.1119	0.1388	0.701	-1.896	>6500	202	3.06	1.39
4905842044993754112	11	0.61753	-60.80400	18.9592	19.0052	18.8705	0.1156	0.0393	0.0763	0.604	-1.689	>6500	160	3.25	1.35
4905839876035355776	12	0.93365	-60.80132	18.9200	19.0192	18.8233	0.1737	0.0912	0.0825	0.577	-1.887	>6500	259	3.17	1.37
4905838123688194048	13	0.75174	-60.86246	20.2184	20.5075	19.8392	0.6504	0.2811	0.3693	0.090	-3.516	5957	141	3.24	1.35
4905647805097805952	15	0.81263	-60.99411	19.0983	19.8099	18.3984	1.3958	0.7024	0.6934	1.568	-2.925	4421	132	2.15	1.57
4905842624814433280	16	0.81460	-60.74894	19.8289	20.1642	19.4524	0.6922	0.3264	0.3658	0.624	-2.582	5840	196	3.05	1.39
4905836233902550656	17	0.58846	-60.97393	19.4989	19.7949	19.0049	0.7739	0.2884	0.4854	0.459	-1.201	5618	81	2.84	1.43
490584346368941312	22	1.03213	-60.74080	19.7344	20.0114	19.4214	0.5695	0.2681	0.3014	1.225	-2.027	6205	210	3.12	1.38
4905839291919803264	23	1.05756	-60.80160	19.8241	20.1851	19.4789	0.6857	0.3518	0.3339	2.820	-3.292	5867	265	3.05	1.39
4905849191820032512	113	0.49597	-60.74761	17.8764	18.2989	17.2878	0.9946	0.4141	0.5805	1.010	-2.166	5094	81	1.99	1.60
4905841632676933376	125	0.84454	-60.77233	20.4191	20.6245	20.2609	0.3427	0.1972	0.1455	-0.285	-1.276	>6500	339	3.61	1.28

Table E.4: Comparison between stars of Grus II in our sample and Simon et al. (2020). The "*" symbol identifies the HB stars. The italic ID identifies the stars whose radial velocity is derived from the blue spectra.

star ID	RA	DEC	v_{rad} [km s $^{-1}$]	$e_{v_{\text{rad}}}$ [km s $^{-1}$]	$v_{\text{rad,Simon}}$ [km s $^{-1}$]	$e_{v_{\text{rad,Simon}}}$ [km s $^{-1}$]	Our member	Member for Simon	[Fe/H]	$\sigma_{[\text{Fe/H}]}$	[Fe/H]_Simon	$\sigma_{[\text{Fe/H}],\text{Simon}}$
<i>1</i> *	331.08387	-46.39487	-98.8	0.5	-108.7	2.4	✓	✓	-	-	-	-
3	330.96673	-46.41297	-107.5	0.4	-109.0	1.3	✓	✓	-2.93	0.12	-2.99	0.28
4	331.01845	-46.42266	-110.3	1.4	-	-	✓	-	-2.93	0.24	-	-
<i>6</i> *	331.14065	-46.44445	-108.0	2.1	-113.2	2.1	✓	✓	-	-	-	-
8	330.88169	-46.53853	-181.9	0.8	-180.5	2.0	✗	✗	-	-	-	-
9	331.06859	-46.37375	-110.3	2.6	-110.2	2.1	✓	✓	-2.92	0.49	-1.82	0.33
10	330.80891	-46.51693	28.2	0.4	28.4	1.2	✗	✗	-	-	-	-
13	331.07562	-46.54788	-106.3	0.9	-107.9	2.0	✓	✓	-2.69	0.18	-	-
<i>14</i> *	330.87292	-46.28101	-104.0	1.2	-	-	✓	-	-	-	-	-
<i>16</i> *	331.21856	-46.35556	-189.7	2.3	-	-	✗	-	-	-	-	-
<i>22</i> *	331.02493	-46.48206	-97.1	1.3	-	-	✓	-	-	-	-	-
23	331.10737	-46.25574	74.9	0.4	-	-	✗	-	-	-	-	-
<i>24</i> *	330.92204	-46.46660	-112.1	1.5	-107.2	2.0	✓	✓	-	-	-	-
25	331.03710	-46.32437	30.1	1.1	31.1	2.7	✗	✗	-	-	-	-
26	331.04160	-46.35068	-107.0	0.3	-108.0	1.1	✓	✓	-2.76	0.07	-2.76	0.17
<i>27</i> *	330.99526	-46.57928	171.1	2.1	-	-	✗	-	-	-	-	-
29	331.00051	-46.42478	-98.3	1.3	-110.9	1.3	✓	✗	-2.24	0.24	-	-
30	330.99051	-46.43441	-108.7	0.7	-109.6	1.3	✓	✓	-2.88	0.17	-2.76	0.25
<i>114</i> *	331.30712	-46.33453	-22.4	1.9	-	-	✗	-	-	-	-	-
121	331.17323	-46.37917	-158.6	0.2	-160.8	1.0	✗	✗	-	-	-	-
122	331.09963	-46.61741	-105.7	0.1	-108.6	1.0	✓	✓	-2.47	0.05	-2.62	0.16

Table E.5: Comparison between stars of Tucana IV in our sample and Simon et al. (2020). The "*" symbol identifies the HB stars. The Δ represents the "unlikely member" stars.

star ID	RA	DEC	v_{rad} [km s $^{-1}$]	$e_{v_{\text{rad}}}$ [km s $^{-1}$]	$v_{\text{rad,Simon}}$ [km s $^{-1}$]	$e_{v_{\text{rad,Simon}}}$ [km s $^{-1}$]	Our member	Member for Simon	[Fe/H]	$\sigma_{[\text{Fe/H}]}$	[Fe/H]_Simon	$\sigma_{[\text{Fe/H}],\text{Simon}}$
3	0.71819	-60.73536	164.4	2.1	162.0	0.70	✗	✗	-	-	-	-
5	0.79783	-60.74766	16.6	0.2	14.7	1.1	✓	-	-1.38	0.07	-	-
<i>6</i> *	0.60930	-60.77164	5.6	2.1	-	-	✓	-	-	-	-	-
7	0.71638	-60.80579	13.5	0.7	9.8	1.5	✓	✓	-2.75	0.17	-2.59	0.30
8	0.73765	-60.86140	16.9	1.4	16.5	2.2	✓	✓	-2.09	0.25	-2.20	0.32
9	0.43461	-60.83191	29.3	1.3	31.7	7.3	Δ	✗	-1.28	0.24	-	-
10*	0.76487	-60.84038	19.6	1.0	18.3	2.5	✓	✓	-	-	-	-
<i>11</i> *	0.61753	-60.80400	14.0	1.3	13.5	3.3	✓	✓	-	-	-	-
<i>12</i> *	0.93365	-60.80132	20.5	1.5	21.1	2.8	✓	✓	-	-	-	-
13	0.75174	-60.86246	-203.8	1.8	-205.4	5.2	✗	✗	-	-	-	-
15	0.81263	-60.99411	143.3	1.1	-	-	✗	-	-	-	-	-
16	0.81460	-60.74894	-18.1	1.7	-19.3	2.6	Δ	✗	-2.46	0.29	-	-
17	0.58846	-60.97393	59.3	1.7	-	-	Δ	-	-2.32	0.29	-	-
22	1.03213	-60.74080	60.3	1.7	-	-	Δ	-	-1.86	0.30	-	-
23	1.05756	-60.80160	125.3	1.9	-	-	✗	-	-	-	-	-
113	0.49597	-60.74761	43.5	0.4	-	-	Δ	-	-1.48	0.11	-	-
<i>125</i> *	0.84454	-60.77233	-40.0	2.5	-	-	Δ	-	-	-	-	-